ANL-6397
Metals, Ceramics, and Materials
(TID-4500, 17th Ed.)
AEC Research and Development Report

ARGONNE NATIONAL LABORATORY
9700 South Cass Avenue
Argonne, Illinois

IRRADIATION OF METAL-FIBER-REINFORCED THORIA-URANIA

by

L. A. Neimark, J. H. Kittel, and C. L. Hoenig*

Metallurgy Division

Final Report - Metallurgy Program 6.2.4

*Now at the Lawrence Radiation Laboratory, Livermore, California

Portions of the material in this report have appeared in the following ANL Metallurgy Division Progress Reports:

ANL-5717	Pages 10-11	March 30, 1957
ANL-5975	Pages 20-21	Dec. 31, 1958
ANL-6330	Page 108	Dec. 31, 1960
ANL-6099	Page 38	Dec. 31, 1959

December 1961

Operated by The University of Chicago
under
Contract W-31-109-eng-38

DISCLAIMER

TABLE OF CONTENTS

LIST OF FIGURES

LIST OF FIGURES

LIST OF FIGURES

LIST OF FIGURES

LIST OF TABLES

IRRADIATION OF METAL-FIBER-REINFORCED THORIA-URANIA

by

L. A. Neimark, J. H. Kittel and C. L. Hoenig

ABSTRACT

Randomly oriented fibers of either molydenum or niobium have been incorporated into hot-pressed pellets of 10, 30, and 50 w/o UO_2 in ThO_2 to improve thermal conductivity and thermal shock resistance. Pellets, 9.5 mm in diameter and 9.5 mm in length, were irradiated in NaK capsules, both bare and jacketed with Zircaloy-2, with the annulus between pellet and jacket filled with lead or helium. They were irradiated to burnups ranging up to 34,500 MWD/T (1.0×10^{21} fiss/cc) at central temperatures of the order of 3000°C. Integral kdθ values ranged from 34 to 129 w/cm.

Fracture and metallographic sections of the irradiated specimens confirmed out-of-pile measurements that the molybdenum fibers increased the effective thermal conductivity of the mixed oxides. It was possible to give the fibered pellets higher heat ratings than unfibered pellets before comparable thermal effects occurred. The fibers tended to reduce central void formation, retard recrystallization, and maintain the integrity of the pellet. In some helium-bonded specimens, the molybdenum fibers coalesced into a central sphere after melting during irradiation. The coalescence did not occur in lead-bonded specimens. The niobium fibers were found to react with the oxide.

Fission gas release from unclad fibered pellets was a maximum of 15.3% of theoretical at a burnup of 31,500 MWD/T (8.3×10^{20} fiss/cc) and an integral kdθ value of 57 w/cm. Gas release from similarly irradiated unfibered pellets was a maximum of 6.3% at 21,800 MWD/T (6.6×10^{20} fiss/cc) and an integral kdθ value of 92 w/cm. The disparity in gas release is attributed to the breaking into pieces of the unfibered pellets early in the irradiation and their consequent operation at significantly lower temperatures than the fibered pellets.

INTRODUCTION

The comparatively low thermal conductivity of oxide fuels has limited the full use of their advantages of dimensional stability, resistance to corrosion, and high melting points. One approach to the problem of increasing the thermal conductivity has been through the addition of thin metal fibers to the oxide matrix. Ideally, the fibers should be radially oriented but, since this is not feasible, the next most advantageous method is random orientation of the fibers. It has been shown that randomly oriented molybdenum fibers in ThO_2 have increased the thermal conductivity by a factor of three in unirradiated material in the temperature range from 250 to 1640°C.(1) It follows from the increased conductivity that the fibered ceramic also has improved resistance to thermal shock.(2) The physical properties of thoria reinforced by metal fibers have been summarized in a recent paper.(3)

The object of this investigation was to evaluate the irradiation characteristics of a fibered oxide fuel body. The effects of the fibers on permissible heat ratings, microstructure, and fission gas release were of primary interest. By cladding the fuel and using either lead or helium bonding, it was possible to evaluate the fibered oxide under different conditions of heat transfer. The fission gas release was determined from capsule-puncture measurements on bare pellets.

Various compositions of ThO_2-UO_2 were chosen as the matrix material for this study. As a nuclear fuel, solid solutions of ThO_2-UO_2 offer the advantages of breeding fissile U^{233}, irradiation stability, and good characteristics for fission product retention.(4-6) The metals selected for use as fibers were molybdenum and niobium. Both have the desirable properties of high melting point, relatively low thermal neutron cross section, and the ability to improve the thermal shock resistance of ThO_2.(7)

FABRICATION

Thoria containing up to 50 w/o urania and additions of metal fibers have been successfully hot pressed into dense bodies.(7) Since it was desired to irradiate fuel with a range of compositions to establish parameters for possible further investigations, the compositions selected for this study were 10,30, and 50 w/o UO_2 in total oxide. The 10 w/o UO_2 addition was 93.2% enriched in U^{235}, whereas the 30 and 50 w/o additions were 19.2% enriched.

The addition of fibrous molybdenum or niobium constituted approximately 10 w/o of the combined oxide-fiber weight. The fibers were all nominally 3.2 mm long with diameters of 0.13 and 0.25 mm for the molybdenum and niobium, respectively.

The UO_2 was reduced from U_3O_8 by hydrogen firing at 800°C for 4 hr. The UO_2 and ThO_2 were mixed in the proper proportions in ball mills for a period of 24 hr. A 0.5 w/o CaF_2 addition was incorporated as a densifying agent. The fibers were intimately mixed with the mixed oxides and the mixture then loaded into a graphite mold. The graphite acted as a susceptor in an induction furnace and also furnished a reducing atmosphere. Molybdenum liners were used to prevent carburization of the niobium.

The specimens were hot pressed into pellets at 1500°C and 175 kg/cm^2 pressure. The pellets were 9.5 mm in diameter, approximately 9.5 mm in length, and weighed between 6.17 and 8.28 gm, of which 0.7 gm was metal fiber. The total porosities ranged from 3.2 to 12.2% of the volume. A few pellets containing no fibers were fabricated for comparison of irradiation effects. The porosity range of these pellets was from 3.8 to 17.4%.

Fourteen irradiation specimens were assembled, each with two pellets of the same composition and fiber content, jacketed in 0.5-mm-thick Zircaloy-2 cladding and a 1.6-mm annulus filled with lead. The pellets were centered by three 1.6-mm-square longitudinal Zircaloy-2 ribs. Six other specimens were assembled with two pellets each in 0.5-mm Zircaloy-2 cladding and a 0.025-mm annulus filled with helium. The end caps on all clad specimens were heliarc welded. Diagrams of the clad specimens are shown in Figure 1.

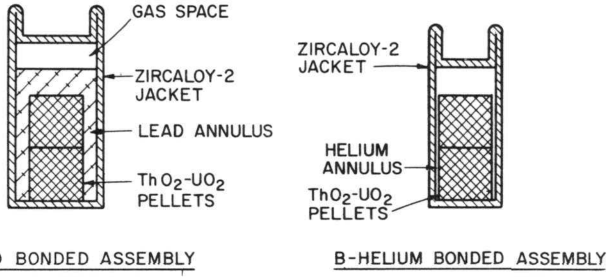

A-LEAD BONDED ASSEMBLY

B-HELIUM BONDED ASSEMBLY

Figure 1. Schematic Vertical Sections of Jacketed Specimens.

IRRADIATION

All specimens, bare and clad, were irradiated singly in aluminum NaK capsules with the space above the NaK evacuated to 0.2 μ Hg. The specimens were loosely held in the capsule in an annulus of stainless steel wool which prevented damage from mechanical shock and also centered the specimen in the capsule. Each capsule contained an aluminum-cobalt flux monitor which was used in determining the burnup and heat output of the specimen.

The capsules were irradiated in the ETR in positions P-9, P-10, and P-11. The irradiation parameters were calculated to give a range of burnups, with a maximum at about 30,000 MWD/T, and maximum central fuel temperatures of 3200°C. From the desired central fuel temperature and the known ETR water-coolant temperature, volumetric rates of heat release were calculated by means of standard equations for heat transfer. For these calculations the thermal conductivity of the unfibered oxide was taken as 0.02 watt/cm-°C and that of the fibered oxide as 0.06 watt/cm-°C, in the temperature range of the irradiation.(1,3) Total perturbation factors were calculated for each composition and enrichment by means of the method by Lewis(8) for MTR-ETR irradiations. The calculation of the unperturbed thermal flux necessary to give the calculated heat generation rate was based on equation 2.164.1 in Glasstone's "Principles of Nuclear Reactor Engineering."(9) The residence times in the reactor of 44, 80, and 127 effective days of irradiation were determined from the desired burnups and calculated thermal neutron flux.

The burnup actually attained by the specimens was calculated from a combination of mass spectrometric analysis of the uranium isotopes and the monitor-indicated thermal flux. A mass spectrometric analysis was obtained for seventeen of the thirty-four specimens. The uranium burnup in each case was calculated from Equation 1, after Kittel and Paine(10):

$$B = F/N_0 = \frac{(a_0 + b_0) - (a + b)}{(1 + \alpha) - (a + b)} \quad . \tag{1}$$

The quantities a_0, a, and b_0, b are the pre- and postirradiation fractions of U^{234} and U^{235}, respectively, N_0 is the original number of atoms of uranium, F is the number of atoms of U^{235} fissioned, B is the total burnup ratio, and α is the ratio of capture to fission cross sections of U^{235}. The basic assumptions are that the burnup is due entirely to U^{235} fissions and that fission accounts for at least 95% of the total uranium lost. For ETR conditions the ratio of capture to fission cross section, α, was taken as 0.185.(11) Since this equation considers only U^{234}, U^{235}, U^{236}, and U^{238} present, it was necessary to normalize the postirradiation analyses, which contained U^{233} from thorium conversion, to these four isotopes. The isotopic analyses before normalizing are given in Table I.

Table I

POSTIRRADIATION URANIUM ISOTOPIC ANALYSES

Specimen No.	U^{233}, w/o	U^{234}, w/o	U^{235}, w/o	U^{236}, w/o	U^{238}, w/o
ANL-35- 3	0.890 ± 0.005	0.143 ± 0.002	14.58 ± 0.10	0.87 ± 0.10	83.51 ± 0.10
- 4	0.853 ± 0.007	0.141 ± 0.001	14.78 ± 0.10	0.847 ± 0.004	83.38 ± 0.10
- 5	10.12 ± 0.06	1.573 ± 0.009	68.21 ± 0.05	11.67 ± 0.07	8.43 ± 0.05
- 6	12.23 ± 0.07	1.72 ± 0.04	63.87 ± 0.05	13.52 ± 0.08	8.66 ± 0.05
- 7	7.08 ± 0.07	1.285 ± 0.008	75.94 ± 0.05	8.28 ± 0.05	7.41 ± 0.05
- 8	0.528 ± 0.003	0.136 ± 0.001	12.85 ± 0.08	1.175 ± 0.007	85.31 ± 0.08
- 9	0.522 ± 0.003	0.140 ± 0.001	13.34 ± 0.08	1.137 ± 0.004	84.86 ± 0.08
-10	0.576 ± 0.004	0.140 ± 0.002	12.75 ± 0.08	1.215 ± 0.007	85.32 ± 0.08
-11	0.368 ± 0.006	0.131 ± 0.002	14.74 ± 0.10	0.873 ± 0.010	83.89 ± 0.10
-12	0.723 ± 0.004	0.138 ± 0.001	15.10 ± 0.09	0.770 ± 0.004	83.27 ± 0.09
-13	0.960 ± 0.006	0.146 ± 0.002	14.81 ± 0.10	0.923 ± 0.006	83.15 ± 0.10
-14	0.732 ± 0.006	0.138 ± 0.001	15.11 ± 0.10	0.784 ± 0.008	83.24 ± 0.10
-15	0.540 ± 0.007	0.135 ± 0.001	16.22 ± 0.01	0.600 ± 0.004	82.50 ± 0.01
-16	1.77 ± 0.01	0.969 ± 0.006	88.80 ± 0.04	2.43 ± 0.02	6.01 ± 0.04
-18	10.9 ± 0.1	1.57 ± 0.01	67.90 ± 0.08	11.3 ± 0.1	8.40 ± 0.08
-23	2.35 ± 0.02	0.213 ± 0.002	9.30 ± 0.09	1.79 ± 0.02	86.30 ± 0.09
-25	0.86 ± 0.01	0.145 ± 0.002	13.7 ± 0.1	1.10 ± 0.01	84.2 ± 0.1

After correcting the cobalt-monitor data for resonance activation, it was assumed that the monitor indicated the true unperturbed thermal flux, since the monitor was located at least 2.5 cm from the specimen. Monitor-indicated burnups were calculated by means of perturbation factors derived from the method by Lewis for MTR-ETR irradiations. From the ratio of mass spectrometric burnup to monitor-indicated burnup, average effective perturbation factors f' were calculated for each of the three compositions that were irradiated. The factors f' were then applied to the monitor-indicated unperturbed fluxes to determine the effective flux for specimens for which analyses were not obtained. A comparison of the calculated perturbation factors and the experimental values of f' is given in Table II. The agreement is generally good.

Table II

CALCULATED AND EXPERIMENTAL PERTURBATION FACTORS

UO_2, w/o	Enrichment, w/o	Calculated f	Experimental f'
10	93.2	0.49	0.56
30	19.2	0.63	0.57
50	19.2	0.48	0.51

Specimens irradiated for 127 days and containing 90 w/o ThO_2 had sufficient U^{233} buildup and subsequent burnup to be significant. The U^{233} burnup was calculated from the work of Taraba.(12)

Tables III, IV, and V summarize the irradiation data. The heat output was calculated from the effective fluxes obtained in the manner described above and with a U^{235} fission cross section of 582 barns and an energy release in the fuel of 180 MeV/fission.

Table III

IRRADIATION BEHAVIOR OF UNCLAD THO_2-UO_2 PELLETS

Specimen No.	UO_2, w/o	Wire Reinforcing	Per Cent Porosity	Days of Irradiation	Burnup		Pellet Surface Heat Flux, watts/cm^2	$\int_{T_s}^{T_o} k d\theta$, w/cm	Fission Gas Release, % Theoretical	Xe/Kr	Condition
					MWD/T Oxide	Fiss/cc (x 10^{20})					
ANL-35-16	10	Mo	8.2	44	7400	1.9	163	34	1.3	7.1	Whole.
- 7	10	None	4.1	127	23,900	7.0	228	47	3.5	6.3	Pellet in pieces.
- 5	10	Mo	4.4	127	31,500	8.3	274	57	15.3	6.6	Pellet in two halves.
- 6	10	None	4.3	127	34,500	10.1	310	64	2.2	5.9	Pellet in pieces.
ANL-35-15	30	None	6.1	44	5900	1.7	176	39	1.4	6.0	Pellet in pieces.
-14	30	None	3.8	44	8200	2.4	196	43	2.9	6.4	Pellet in pieces.
-12	30	Mo	5.2	80	8200	2.2	120	27	4.5	7.3	Whole.
-13	30	Mo	9.6	44	8700	2.2	207	46	8.1	7.1	Pellet in two halves.
- 4	30	Nb	6.9	44	8800	2.3	209	47	7.6	5.8	Large transverse fissure at midplane.
- 3	30	Nb	5.5	44	9200	2.4	228	51	8.1	7.2	Large transverse fissure at midplane.
ANL-35-11	50	None	6.8	80	15,200	4.4	225	48	3.2	7.6	Pellet in pieces.
- 9	50	Mo	5.9	80	19,800	5.3	289	61	8.1	7.8	Pellet in two halves.
- 8	50	Mo	4.3	127	21,500	5.7	193	41	15.0	9.5	Pellet in two halves.
-10	50	None	4.4	80	21,800	6.6	440	92	6.3	6.9	Pellet in pieces.

Table IV

IRRADIATION BEHAVIOR OF LEAD-BONDED ZIRCALOY-2-CLAD ThO_2-UO_2 PELLETS

Specimen No.	UO_2 w/o	Wire Reinforcing	Per Cent Porosity[a]	Days of Irradiation	Burnup		Cladding Surface Heat Flux, watts/cm^2	$\int_{T_s}^{T_o} k\,d\theta$, w/cm	Maximum Diameter Change, %	Volume Increase, %	Cladding Condition
					MWD/T Oxide	Fiss/cc (x 10^{20})					
ANL-35-20	10	None	6.4 6.3	127	20,000	5.8	254	67	+1.4	0.0	(b)
-19	10	Mo	7.0 7.8	127	28,700	7.4	431	115	+1.5	0.6	(b)
-18	10	Mo	6.5 7.0	127	29,700	7.7	460	122	+1.6	1.8	(b)
-17	10	Mo	3.2 7.4	127	31,100	8.2	482	129	+15.2	-	Four holes and one long crack.
ANL-35-24	30	None	5.4 17.4	44	4900	1.4	189	54	+0.1	0.0	(b)
-22	30	Mo	4.4 8.7	44	7100	1.9	291	83	+0.1	0.0	(b)
-29	30	Nb	4.9 7.8	44	8000	2.1	279	79	0.0	0.1	(b)
-21	30	Mo	4.5 6.9	44	8200	2.2	351	100	-1.0	0.0	(b)
-30	30	Nb	5.3 4.6	80	12,100	3.2	272	77	-0.6	0.1	(b)
-23	30	Mo	4.7 9.4	127	20,500	5.1	352	100	+1.8	0.4	(b)
ANL-35-28	50	None	6.3 3.8	80	11,300	3.4	253	68	-0.1	0.1	(b)
-27	50	Mo	7.5 7.4	80	13,600	3.6	284	76	+0.2	0.2	(b)
-26	50	Mo	4.3 5.4	80	17,000	4.6	357	96	0.0	0.2	(b)
-25	50	Mo	12.2 6.0	80	18,800	5.0	403	110	-0.3	0.4	(b)

(a) Top value refers to top pellet in assembly, bottom value to bottom pellet.

(b) Cladding unmarked.

Table V

IRRADIATION BEHAVIOR OF HELIUM-BONDED ZIRCALOY-2-CLAD ThO_2-UO_2 PELLETS

Specimen No.	UO_2, w/o	Wire Reinforcing	Per Cent Porosity[a]	Days of Irradiation	Burnup		Cladding Surface Heat Flux, watts/cm^2	$\int_{T_s}^{T_o} k\,d\theta$, w/cm	Maximum Diameter Change, %	Volume Increase, %	Cladding Condition
					MWD/T Oxide	Fiss/cc (x 10^{20})					
ANL-35-32	10	Mo	8.5 5.2	127	27,100	7.0	500	100	+9.3	-	Large melt hole.
-31	10	Mo	4.1 3.8	127	27,800	7.4	536	107	+6.5	1.8	Blister and melt spot.
ANL-35-33	30	Mo	11.7 6.5	44	6100	1.6	343	73	+0.2	0.4	No change.
-34	30	Mo	5.7 10.3	44	6800	1.8	365	78	+0.4	0.9	Large melted area.
ANL-35-35	50	Mo	6.4 5.6	80	16,700	4.4	480	97	+1.4	-	Large melt hole.
-36	50	Mo	9.8 6.6	80	17,400	4.5	508	103	+7.7	-	Very large melt hole.

(a) Top value refers to top pellet in assembly, bottom value to bottom pellet.

Maximum radial heat flow was taken as 44 and 86% of the heat output from single pellets and clad specimens, respectively.(13) The calculation of accurate internal temperatures was not possible because of the uncertainty of the thermal conductivity. Adding to this difficulty was the high probability of boiling of NaK at the pellet or cladding surfaces, making a rigorous temperature calculation virtually impossible. Temperatures were therefore estimated from the condition of the molybdenum or niobium fibers or of the Zircaloy-2 supporting ribs.

The values of the heat rating $\int_{T_s}^{T_0} k d\theta$ were derived from the maximum radial heat ratings by the equation

$$\int_{T_s}^{T_0} k d\theta = qF/4\pi \quad , \qquad (2)$$

where

q = radial heat output (watt/cm)

F = a factor taking into account nonuniform heat generation in a neutron-depressing fuel.

The equation is from the work of Robertson(14) in which F is defined as a function of fuel enrichment, diameter, density, and the energy spectrum of the reactor. Because of uncertainties in the latter quantity for our specimens, a rigorous calculation of F was not possible. With reservations and realizing that a slight inherent error exists, the factor F was taken from Figure 2 in CRFD-835 after modifying the abscissa to "grams U^{235} per cc." The calculated values of the integral are consistent within themselves and would not differ significantly from those obtained from a rigorous calculation of F.

POST IRRADIATION EXAMINATION

Visual Observations

The cladding of one-lead bonded specimen, ANL-35-17 (see Figure 2) had melted and undergone extensive swelling and rupture.

25200 2X

Figure 2. Lead-bonded, Molybdenum-fibered Specimen ANL-35-17 after a Burnup of 31, 100 MWD/T and an Integral kdθ Value of 129 w/cm Showing Cladding Burnout and Longitudinal Crack.

The cladding on all other lead-bonded specimens was unaffected. An undamaged lead-bonded specimen, ANL-35-18, is shown in Figure 3. The cladding on five of the six helium-bonded specimens had melted through or had begun to melt. Figures 4, 5 and 6 show typical damage to the helium-bonded specimens. The exposure of the fuel to the NaK caused significant losses of fuel from both the lead- and helium-bonded specimens.

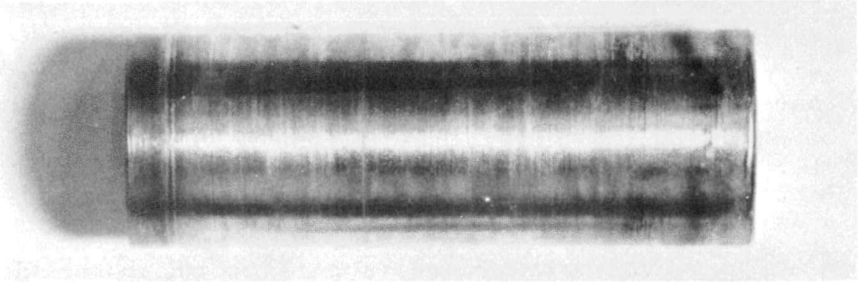

25201 2X

Figure 3. Lead-bonded, Molybdenum-fibered Specimen ANL-35-18 after a Burnup of 29,700 MWD/T and an Integral kdθ Value of 122 w/cm Showing No Visible Cladding Defects.

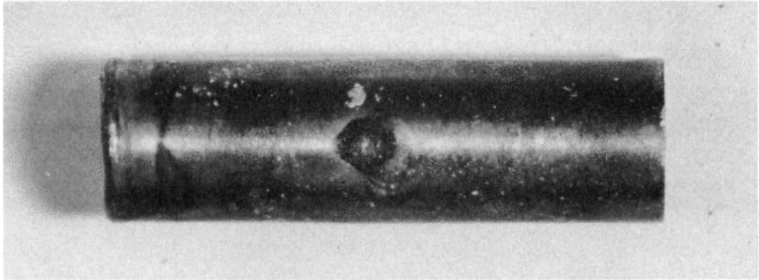

25032 2X

Figure 4. Helium-bonded, Molybdenum-fibered Specimen ANL-35-34 after a Burnup of 6800 MWD/T and an Integral kdθ Value of 78 w/cm Showing a Melted Region on Cladding Surface.

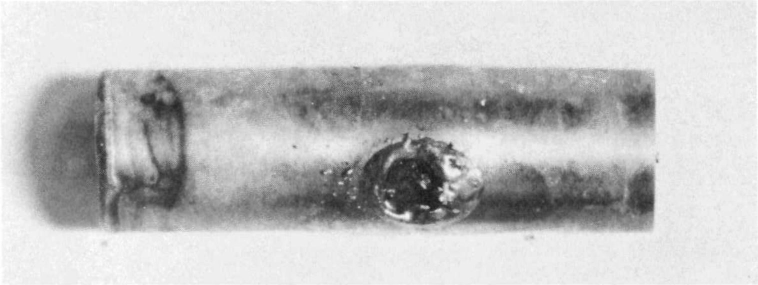

25208 2X

Figure 5. Helium-bonded, Molybdenum-fibered Specimen ANL-35-32 after a Burnup of 27,100 MWD/T and an Integral kdθ Value of 100 w/cm Showing Cladding Burnout Failure.

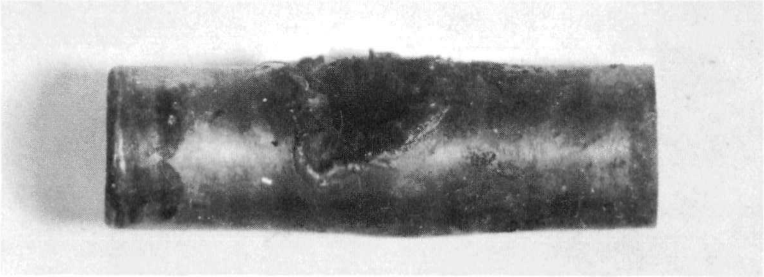

25037 2X

Figure 6. Helium-bonded, Molybdenum-fibered Specimen ANL-35-36 after a Burnup of 17,400 MWD/T and an Integral kdθ Value of 103 w/cm Showing Cladding Burnout and Exposed Fuel.

The capsules containing the bare pellets were punctured for fission gas measurements and the pellets then removed. All pellets without fibers had broken into many small fragments. The fibered pellets broke into no more than two or three pieces, usually at the midplane, and in two instances remained whole. The appearances of typical unclad pellets are shown in Figures 7 through 10.

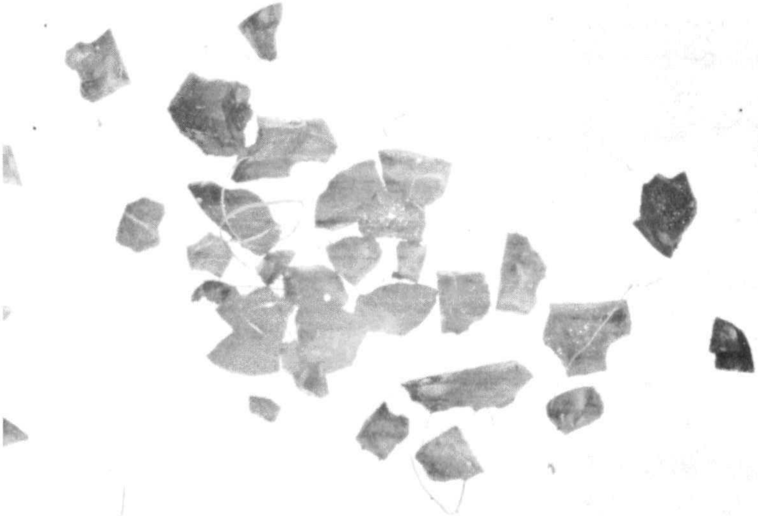

28161 2X

Figure 7. Specimen ANL-35-14 after a Burnup of 8200 MWD/T, Showing Fracturing of Unclad, Unfibered Pellet.

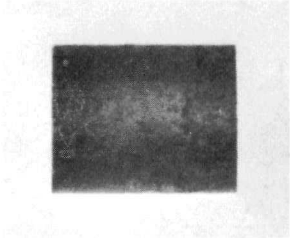

Figure 8

Unclad, Molybdenum-fibered Pellet, Specimen ANL-35-12, Showing No Change after a Burnup of 8200 MWD/T and an Integral kdθ Value of 27 w/cm.

28159 2X

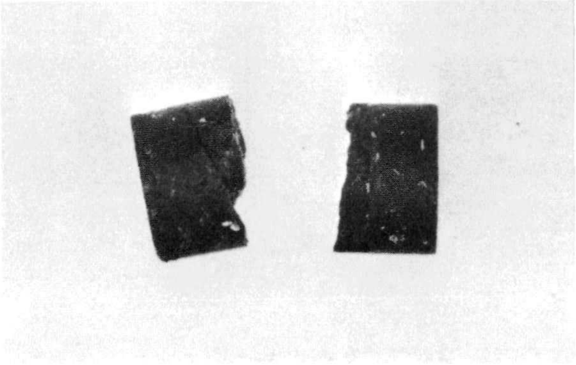

28155 2X

Figure 9. Specimen ANL-35-8 after a Burnup of 21,500 MWD/T and an Integral kdθ Value of 41 w/cm, Showing Maximum Damage Received by an Unclad, Molybdenum-fibered Pellet.

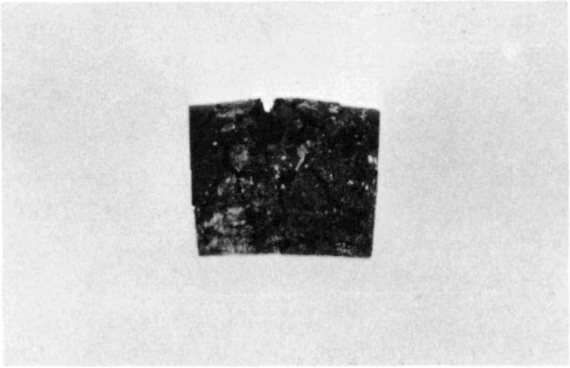

28150 2X

Figure 10. Specimen ANL-35-3 after a Burnup of 9200 MWD/T and an Integral kdθ Value of 51 w/cm, Showing Typical Damage Received by Unclad, Niobium-fibered Pellets.

Dimensional and Density Measurements

Diameter measurements were made on the clad specimens with a standard micrometer. Duplicate measurements were obtained by analysis of 2X photographs containing a diameter standard. The diameter changes as measured ranged from -1.0% to +15.2% for lead-bonded specimens and from +0.2% to +9.3% for helium-bonded specimens. The precision of the postirradiation measurements was at best ±0.05 mm, or about ±0.4%. Since swelling and blistering were not uniform, it was not always possible to ascertain the maximum diameter change with either the micrometer or the photographs. A truer indication of specimen swelling was obtained from volume changes calculated from density measurements.

Densities of unruptured clad specimens were determined by a CCl_4 immersion technique using a 200-gm Mettler analytical balance. Volume changes were obtained by correcting the densities to zero weight change. The volume increases ranged from zero to 1.0% for lead-bonded specimens and from 0.4% to 1.8% for helium-bonded specimens. The error in the volume determinations was less than 0.1%. The volume increases of lead-bonded ANL-35-18 and helium-bonded ANL-35-31, 1.0% and 1.8%, respectively, are significant because these specimens attained the highest heat ratings without failure. It appears that lead-bonded assemblies have less tendency to swell before failure than do helium-bonded assemblies, and at significantly higher heat ratings.

A summary of the dimensional changes is found in Tables IV and V.

Fission Gas Release

The fourteen capsules containing the bare pellets were punctured for gas measurement in a modified arbor press arrangement. The press was fitted with a spring-loaded, vacuum-tight bellows which surrounded a stationary, three-faced tool steel needle. The capsule was placed in an aluminum block holder which was then seated in the press so that the puncturing needle was aligned with the center of the capsule. A vacuum O-ring seal was made between the aluminum holder and the bottom supporting block of the bellows and a vacuum of 10μ or less was drawn around the capsule. The fission gases that escaped from the fuel to the evacuated space above the NaK were released to an evacuated collection system when the needle pierced a 1.0-mm-thick aluminum membrane at the top of the capsule. The gas diffused through a 9.5-mm-diameter copper tube connected to the aluminum holder and out of the hot cell to the collection system. After equilibrium had been attained, in about 30 min, the pressure in the known volume of the system was measured by either of two tilting McLeod gages depending on the magnitude of the pressure. A 0.5-cc sample of the gas was transferred to a collection bulb by a mercury diffusion pump and taken for mass spectrometric analysis. The gas remaining in the system was statically trapped in a bulb containing activated charcoal and cooled to liquid nitrogen temperature. The puncturing apparatus and collection system are shown in Figures 11 and 12.

The volume of fission gas released from the fuel was calculated from the pressure-volume relationship and the xenon and krypton isotopic analyses. The four isotopes of xenon analyzed were Xe^{131}, Xe^{132}, Xe^{134}, and Xe^{136}. The Xe^{136} fraction was partly from fission and partly from neutron capture by Xe^{135}. In the neutron flux to which the specimens were exposed, about 10^{14} n/cm^2-sec, it was calculated that about 94% of the Xe^{135} went to Xe^{136}.

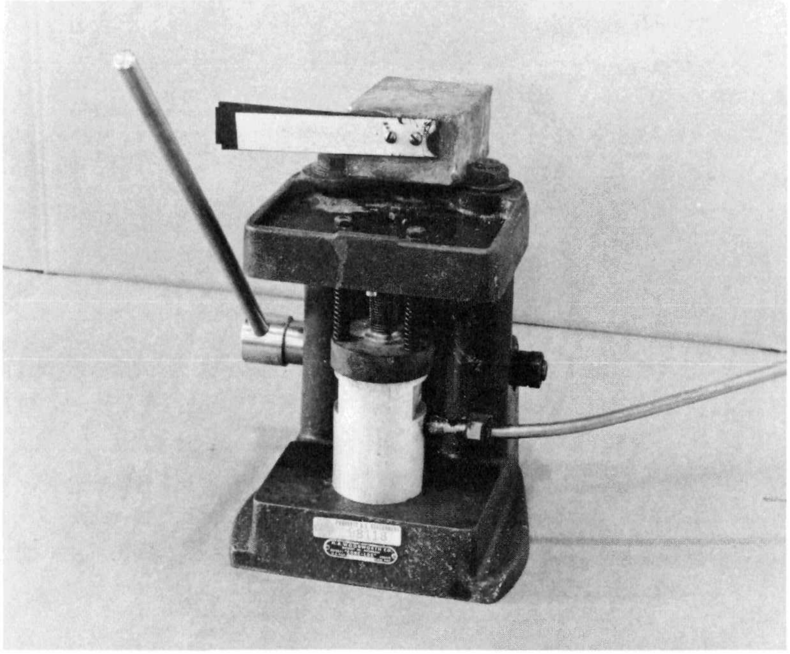

EI-12

Figure 11. Capsule Puncturing Apparatus for Fission Gas Measurements

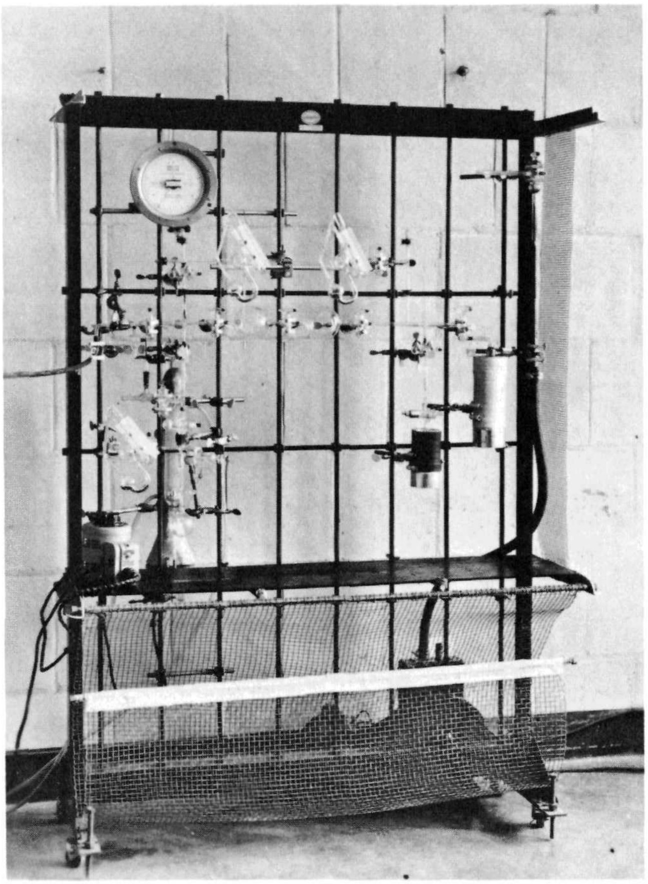

EI-13

Figure 12. Fission Gas Collection and Measurement Apparatus

The total U^{235} fission yield for xenon that was used in calculating the theoretical gas release, including the Xe^{136} from Xe^{135}, was 27.6%. The fission yield for krypton was taken as 3.8%. For U^{233} fission, the yields used were 26.2% and 7.0% for xenon and krypton, respectively.(15) The results of the theoretical calculations for gas release are included in Table III. The results are also plotted as functions of burnup and $\int_{T_s}^{T_0} k d\theta$ in Figures 13 and 14.

The ratio of xenon to krypton in the escaped gases fell within the range from 5.9 to 7.8 with the exception of ANL-35-8, for which it was 9.5. The trend was toward an increasing ratio of xenon to krypton with increasing UO_2 content. The scatter in the theoretical release data is partly attributed to this changing ratio and partly to the inconsistent densities. The high ratio of xenon to krypton of ANL-35-8 is considered anomalous with the other data.

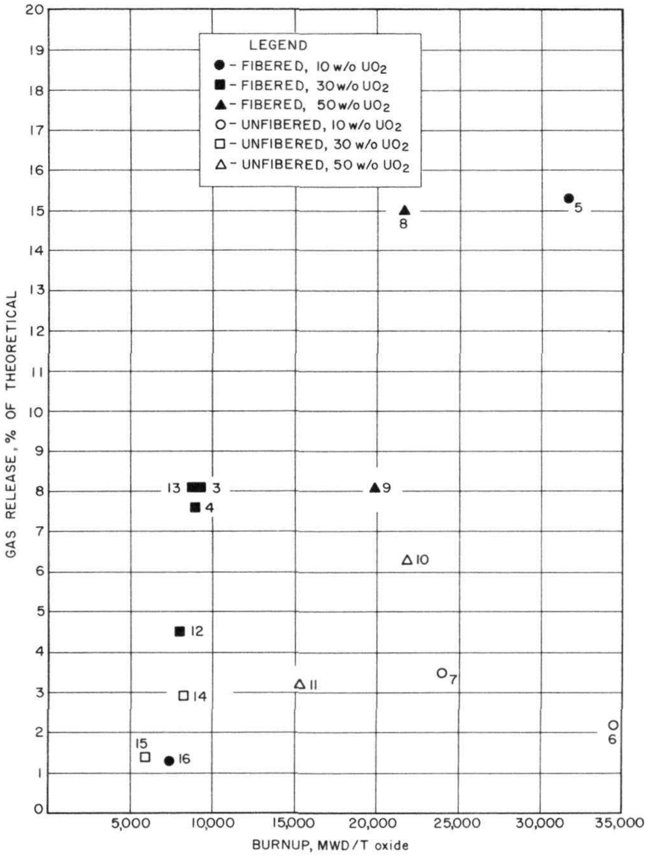

Figure 13

Fission Gas Release as a Function of Burnup. Numbers Refer to Specimen Identification as Given in Table III.

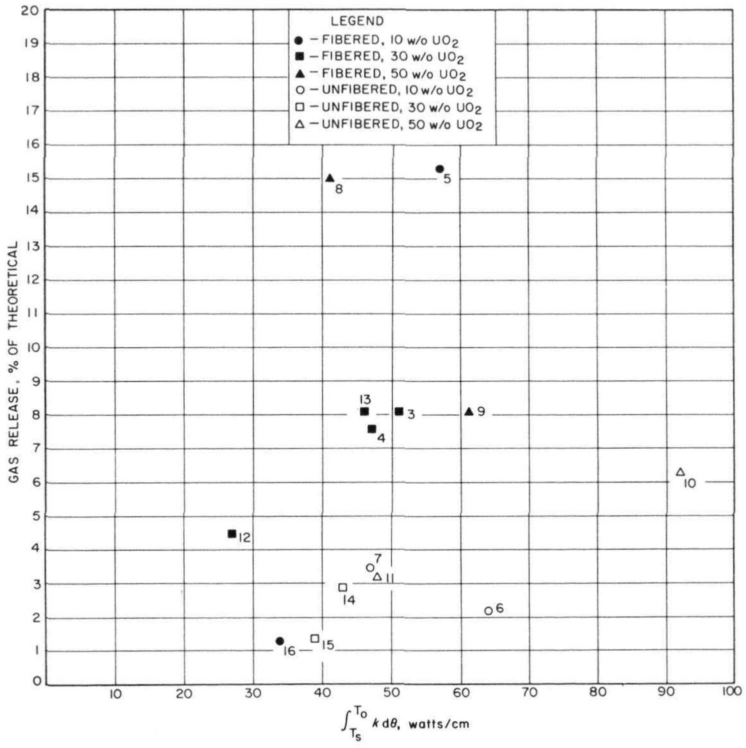

Figure 14. Fission Gas Release as a Function of $\int_{T_s}^{T_o} kd\theta$. Numbers Refer to Specimen Identification as Given in Table III.

Metallography

Since the total length of the pellets in the clad specimens was considerably less than the total free space, it was necessary to locate the pellets in the cladding before sectioning. A technique was developed in which the specimens were placed on an X-ray film packet which was then removed from the hot cell and developed. Typical autoradiographs are shown in Figure 15. It was evident that the two pellets had not remained together in all specimens. With the radiographs as a guide, the specimens were sectioned with a tubing cutter as near as possible to the midplane of each pellet. Subsequent examination showed that in a few cases the cladding was distorted during cutting because of the difficulty in cutting through the spacing ribs in the lead-bonded specimens. Figures 16 through 25 show typical fracture sections of the clad specimens.

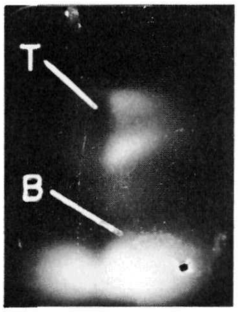

27396 1X

ANL-35-21

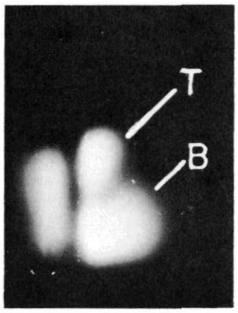

27397 1X

ANL-35-27

Figure 15

Autoradiographs of Specimens ANL-35-21 and ANL-35-27 Showing Variation in Top and Bottom Pellet Separation in Lead-bonded Assemblies after Irradiation.

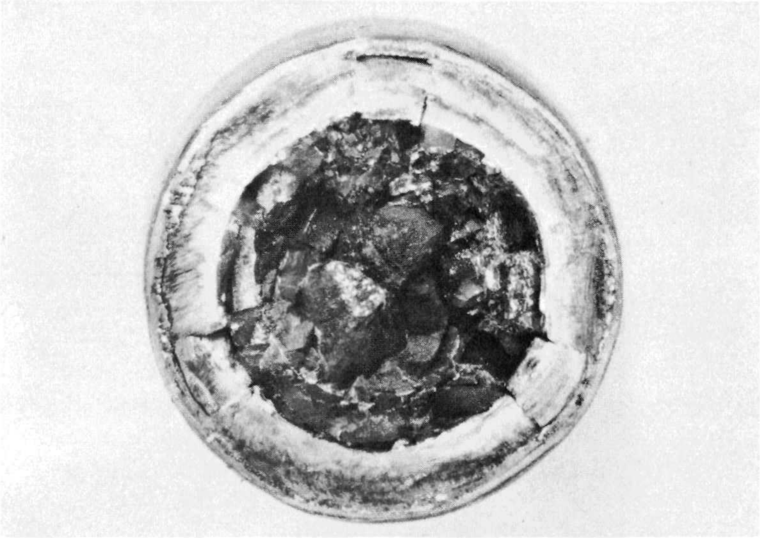

26931 5X

Figure 16. Fracture Surface of Bottom Pellet in Unfibered, Lead-bonded Specimen ANL-35-24, Showing Cracking after a Burnup of 4900 MWD/T and an Integral kdθ Value of 54 w/cm.

26973 5X

Figure 17. Fracture Surface of Bottom Pellet in Unfibered, Lead-bonded Specimen ANL-35-28, Showing Radial Columnar Grains and a Small Central Void Filled with Lead after a Burnup of 11,300 MWD/T and an Integral kdθ Value of 68 w/cm.

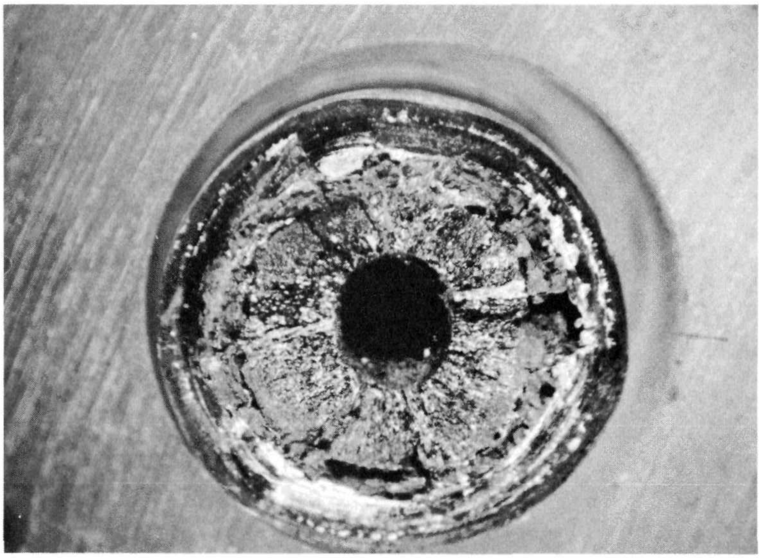

25668 5X

Figure 18. Fracture Surface of Top Pellet in Unfibered, Lead-bonded Specimen ANL-35-20, Showing Radial Columnar Grains and Central Void after a Burnup of 20,000 MWD/T and an Integral kdθ Value of 67 w/cm.

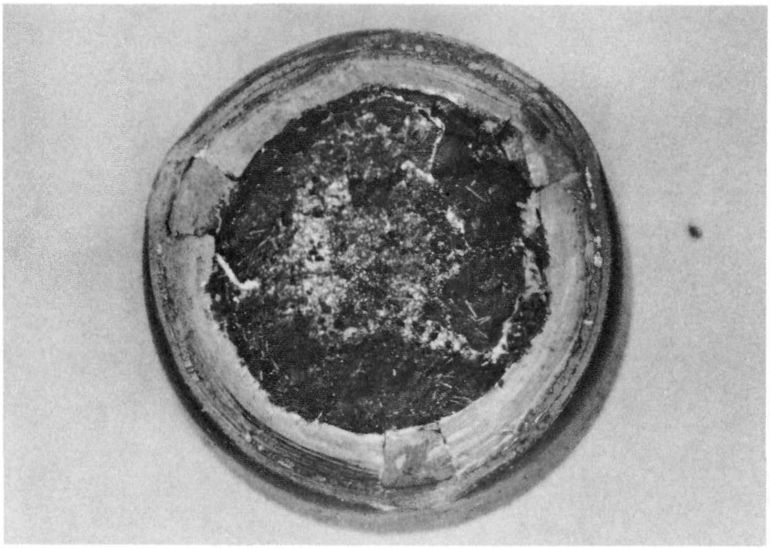

26965 5X

Figure 19. Fracture Surface of Bottom Pellet in Molybdenum-fibered, Lead-bonded Specimen ANL-35-22, Showing Some Melted Fibers but no Central Void after a Burnup of 7100 MWD/T and an Integral kdθ Value of 83 w/cm.

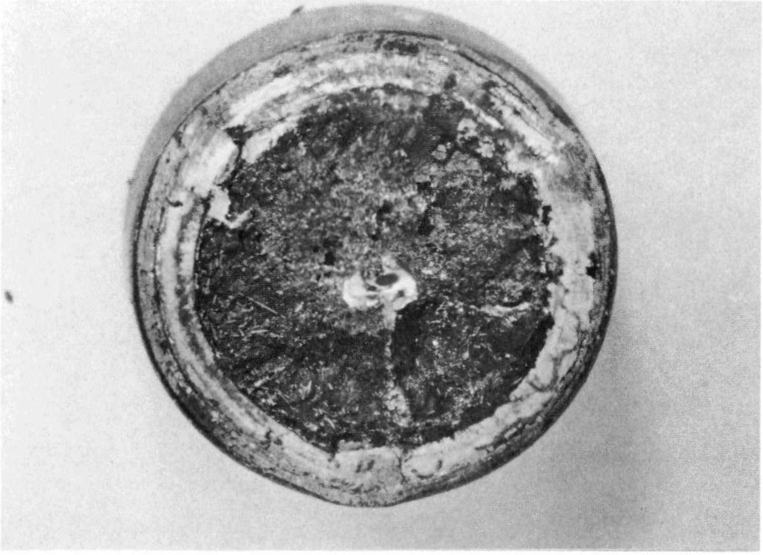

26935 5X

Figure 20. Fracture Surface of Bottom Pellet in Molybdenum-fibered, Lead-bonded Specimen ANL-35-26, Showing Area Just Below Small Central Void after a Burnup of 17,000 MWD/T and an Integral kdθ Value of 96 w/cm.

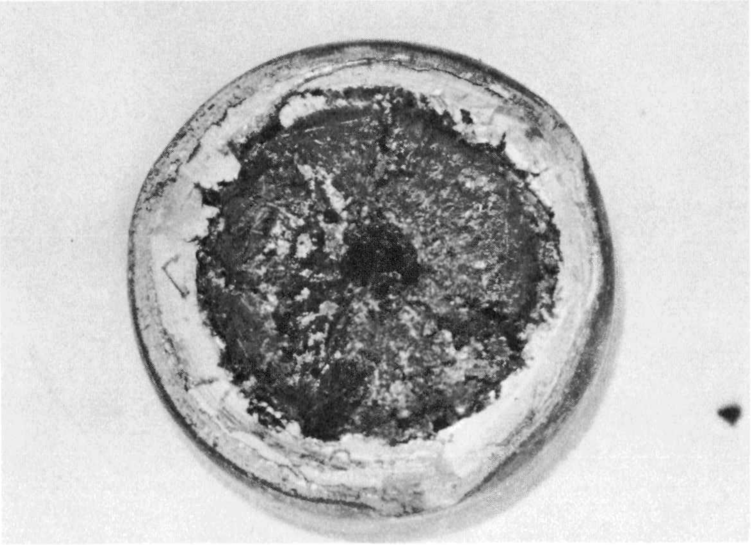

26967 5X

Figure 21. Fracture Surface of Bottom Pellet in Molybdenum-fibered, Lead-bonded Specimen ANL-35-23, Showing Central Void, Melted Fibers, and Beginnings of Columnar Recrystallization after a Burnup of 20,500 MWD/T and an Integral kdθ Value of 100 w/cm.

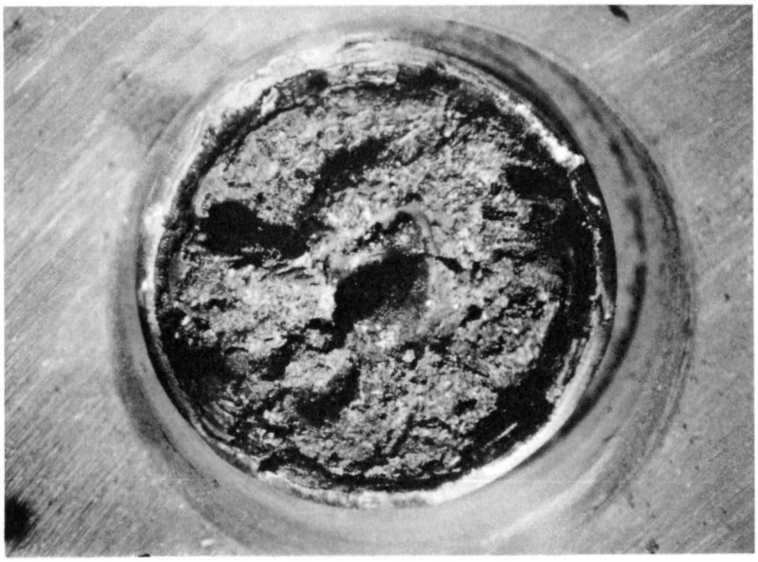

25674 5X

Figure 22. Fracture Surface of Bottom Pellet in Molybdenum-fibered, Lead-bonded Specimen ANL-35-18, Showing Mixture of Lead and Oxide after a Burnup of 29,700 MWD/T and an Integral kdθ Value of 122 w/cm.

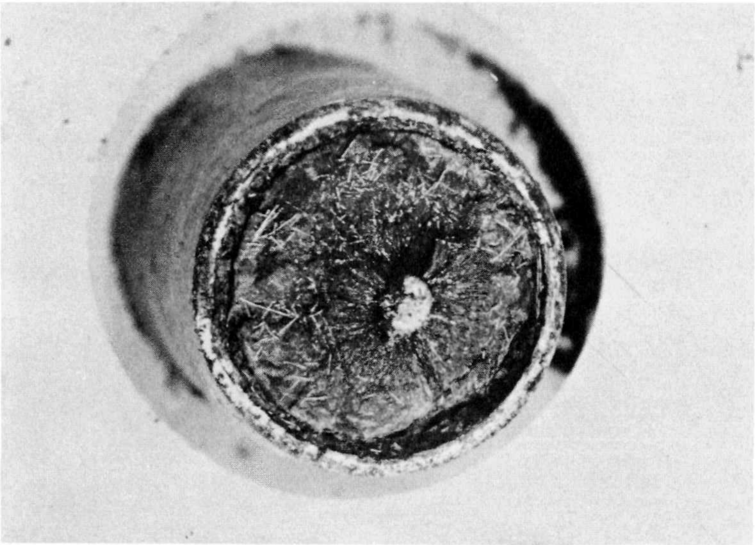

26984 5X

Figure 23. Fracture Surface of Top Pellet in Molybdenum-fibered, Helium-bonded Specimen ANL-35-34, Showing Small Metal Bead Surrounded by Small Columnar Grains after a Burnup of 6800 MWD/T and an Integral kdθ Value of 78 w/cm.

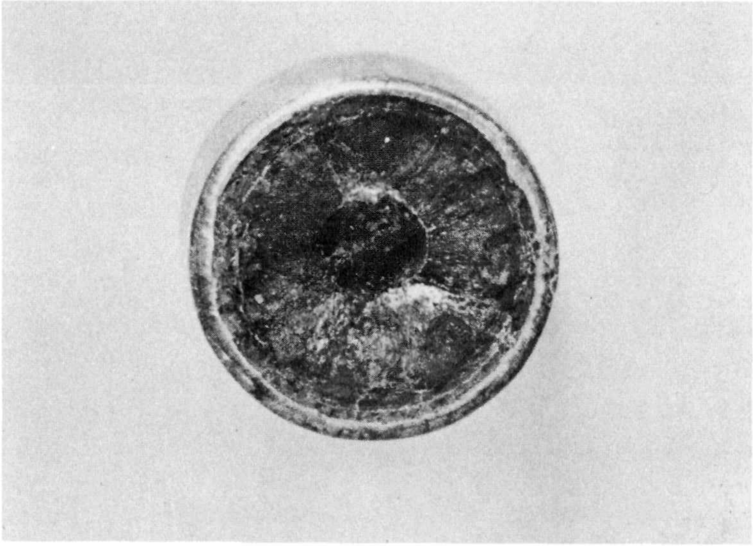

26982 5X

Figure 24. Fracture Surface of Bottom Pellet in Molybdenum-fibered, Helium-bonded Specimen ANL-35-32, Showing Columnar Grains Surrounding a Central Void Containing Melted Fibers after a Burnup of 27,100 MWD/T and an Integral kdθ Value of 100 w/cm.

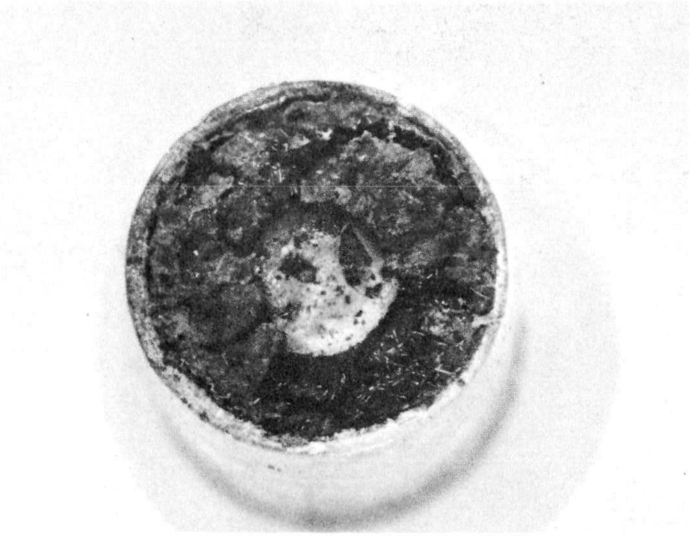

26980 5X

Figure 25. Fracture Surface of Bottom Pellet in Molybdenum-fibered Helium-bonded Specimen ANL-35-31, Showing Large Central Metal Bead Surrounded by Columnar Grains after a Burnup of 27,800 MWD/T and an Integral kdθ Value of 107 w/cm.

The fracture sections of clad specimens, halves of fibered bare pellets, and randomly oriented pieces of unfibered bare pellets, were mounted in cold-setting Hysol 6040 epoxy resin. Rough grinding was done successively on 80, 120, 320, and 600-grit silicon carbide papers lubricated with "OS" Hyprez fluid. Polishing was done on silk cloths using 3- and 1-micron diamond paste with final polishing on Microcloth impregnated with $\frac{1}{4}$-micron diamond paste and all using "OS" Hyprez lubricant. Attempts at etching with hot and cold solutions of 10 parts HNO_3 and 1 part HF or 9 parts H_2SO_4 and 1 part 30% H_2O_2 produced only etch pits. It was believed that the low grinding and polishing pressures, 350 and 125 grams, respectively, and the slow turntable speeds of 160 rpm were successful in bringing out most of the grain structure that was present. All the metallographic sections presented here are therefore in the as-polished condition.

Random pieces from the unfibered, unclad pellets had relatively few and small areas of recrystallization, as shown in Figure 26. This would indicate that these specimens were irradiated at low temperature caused by their breaking up and having a very large surface area exposed to the NaK coolant. What appeared to be a light gray second phase was present in all specimens, clad and unclad, regardless of burnup or composition. In the unclad pellets this phase was not homogeneous and gave the ceramic a "patchy" appearance. Some pieces exhibited a white band at what probably was once the circumference. The band was free of the second phase, as were the recrystallized areas.

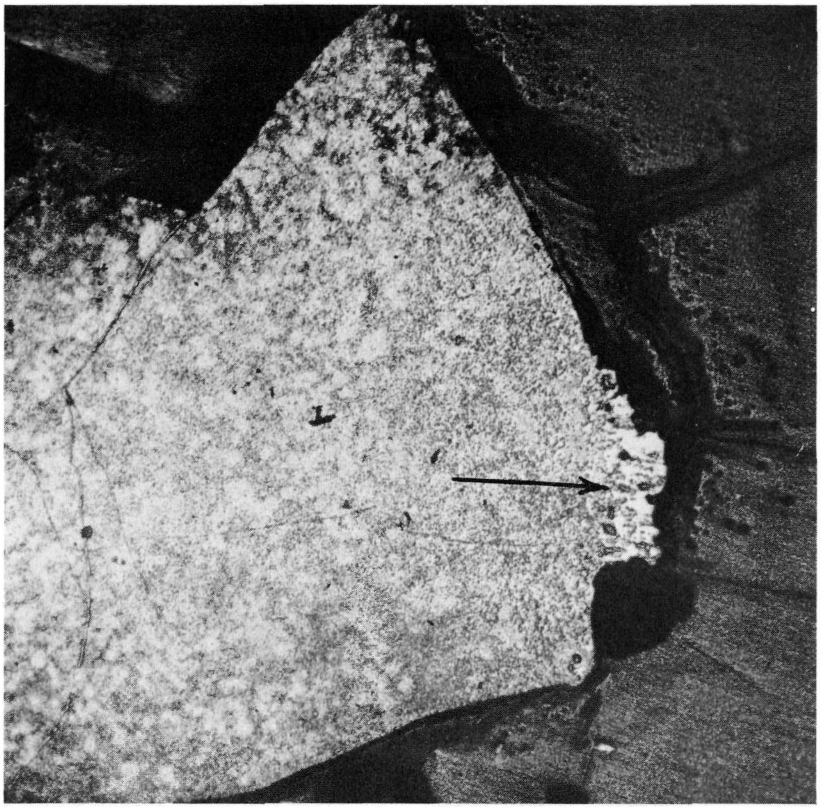

31447

50X

Figure 26. Randomly Oriented Fragment from Unfibered Specimen ANL-35-6, Showing "Patchy" Second Phase (Dark) and a Small Recrystallized Area on the Right Extremity (Arrow). Average Temperature of Irradiation Was Low.

The unclad fibered pellets, which did not break up as readily as the unfibered pellets, showed thermal effects ranging from no apparent change, as in Figure 27, to slight central recrystallization, as in Figure 28, to a central void surrounded by some recrystallization, as in Figure 29. Some pores near the center of ANL-35-5 were platelike and perpendicular to the radius. They were present at the ends of radially oriented grains. A typical platelet void is shown in Figure 30. Cracking was randomly oriented and did not form a network between fibers.

The niobium fibers in both the clad and unclad specimens reacted with either the oxide or the atmosphere present in the pellet. Reactive gases in the pellet would include excess oxygen from nonstoichiometric UO_2 and hydrogen that was chemisorbed on the UO_2 during the reduction from U_3O_8. Molybdenum reactions with the environment were not evident. Some typical niobium reactions are shown in Figures 31, 32, and 33. An unreacted molybdenum fiber is shown in Figure 34.

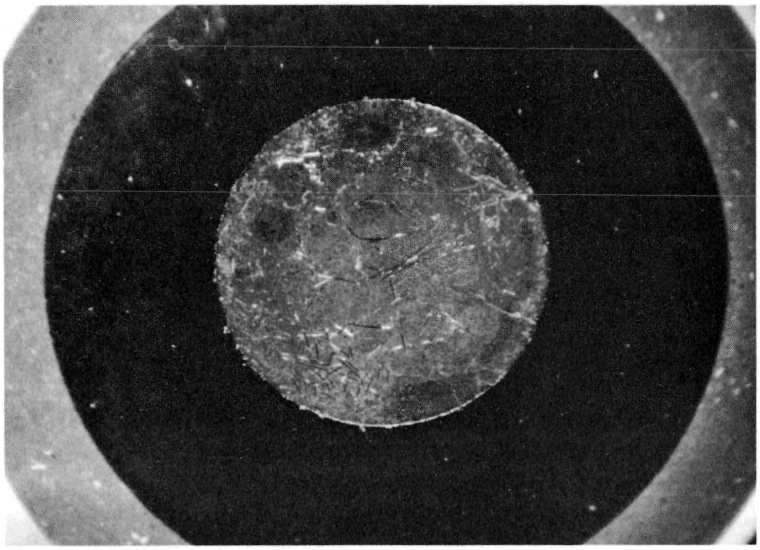

31437 5X

Figure 27. Polished Section of Specimen ANL-35-16. Molybdenum Fibers Are Discernible after 7400 MWD/T at an Integral kdθ Value of 34 w/cm.

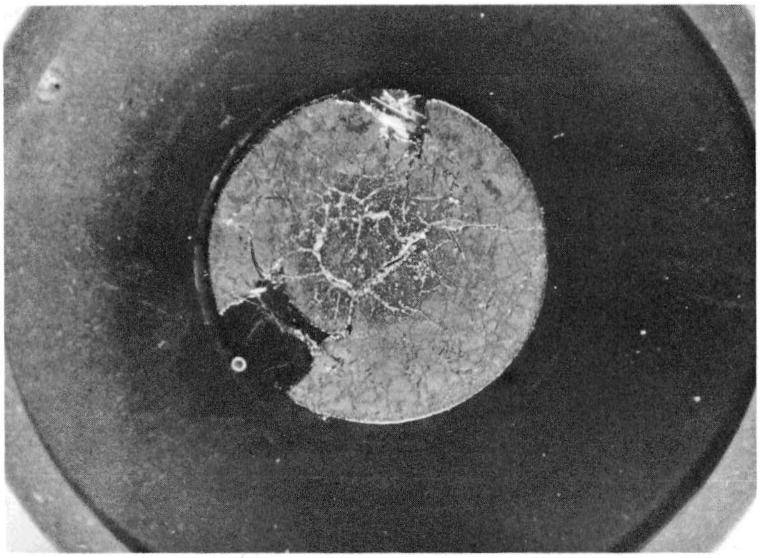

31436 5X

Figure 28. Polished Section of Molybdenum-fibered Specimen ANL-35-13. Central Area Has Begun to Recrystallize after 87000 MWD/T at an Integral kdθ Value of 46 w/cm.

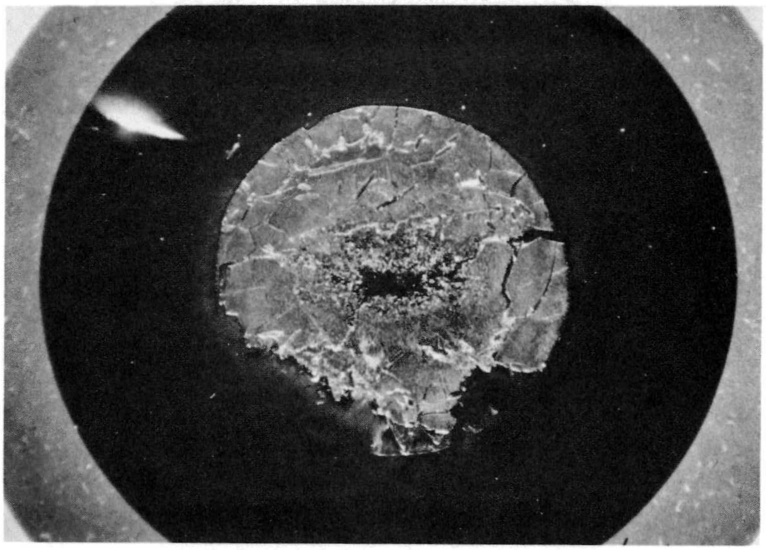

31431 5X

Figure 29. Polished Section of Niobium-fibered Specimen ANL-35-4. Central Void and Some Recrystallization Has Occurred after 8800 MWD/T at an Integral kdθ Value of 47 w/cm.

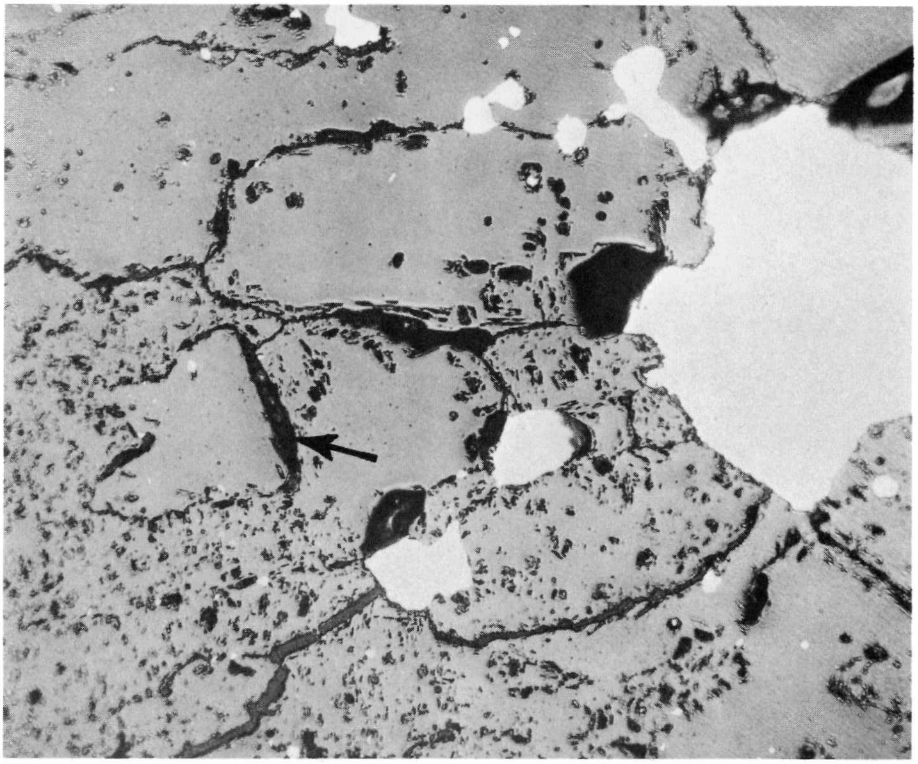

31424 250X

Figure 30. Beginning Movement of Platelet Void (Arrow) Toward Center of Specimen ANL-35-5. White Areas Are Melted Molybdenum Fibers.

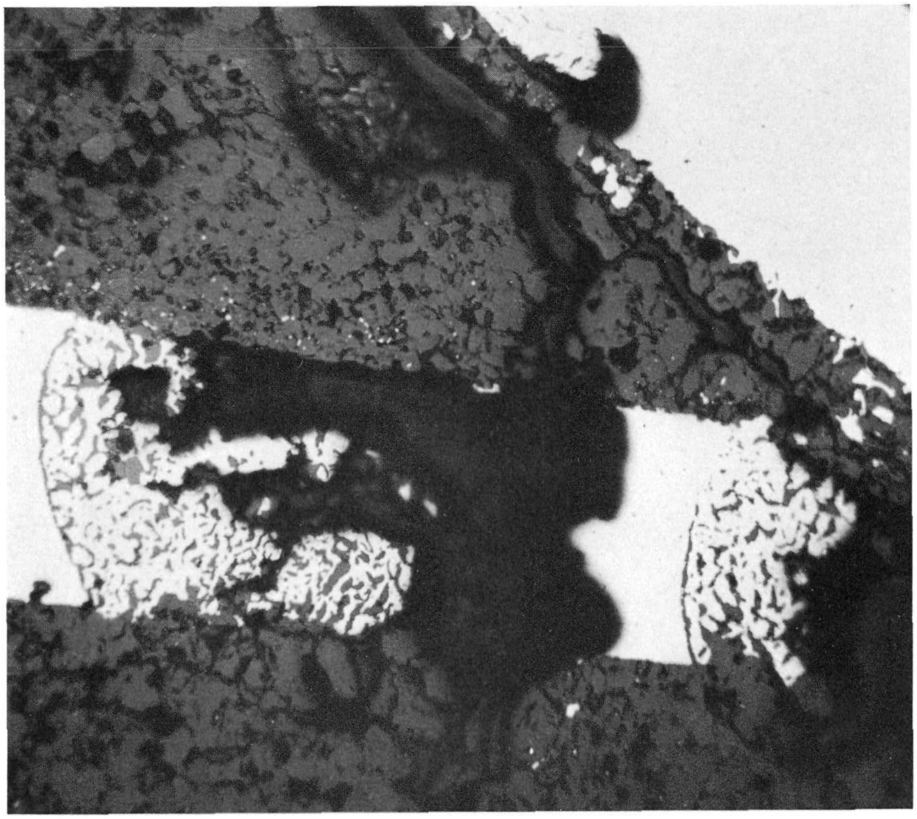

31378 250X

Figure 31. Niobium-fiber Reaction in Unclad Specimen ANL-35-4.

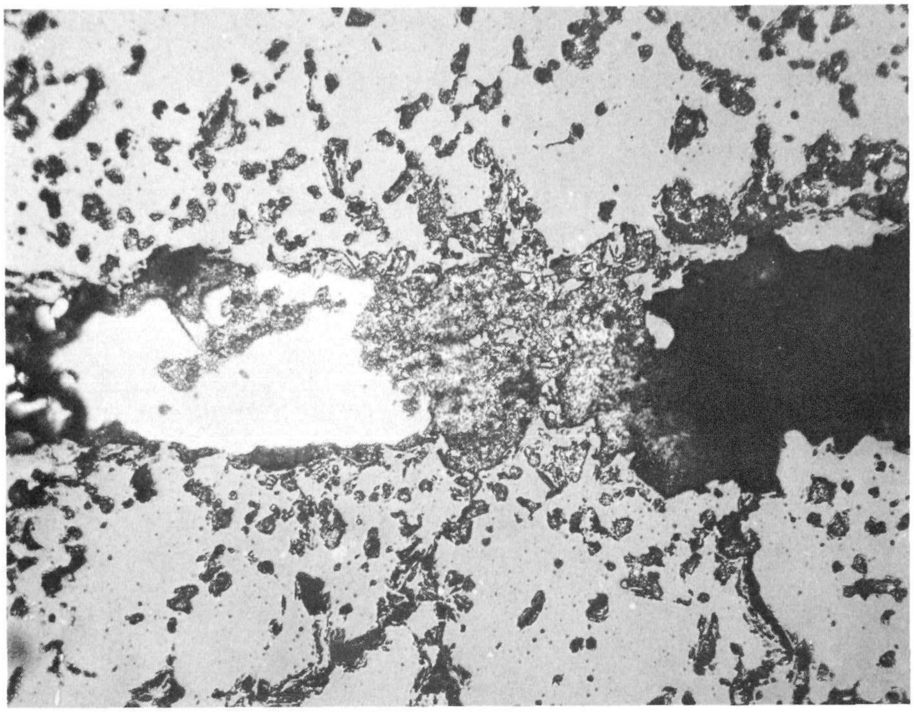

31293 250X

Figure 32. Remains of Niobium Fiber and Reaction Product in Lead-bonded Specimen ANL-35-29.

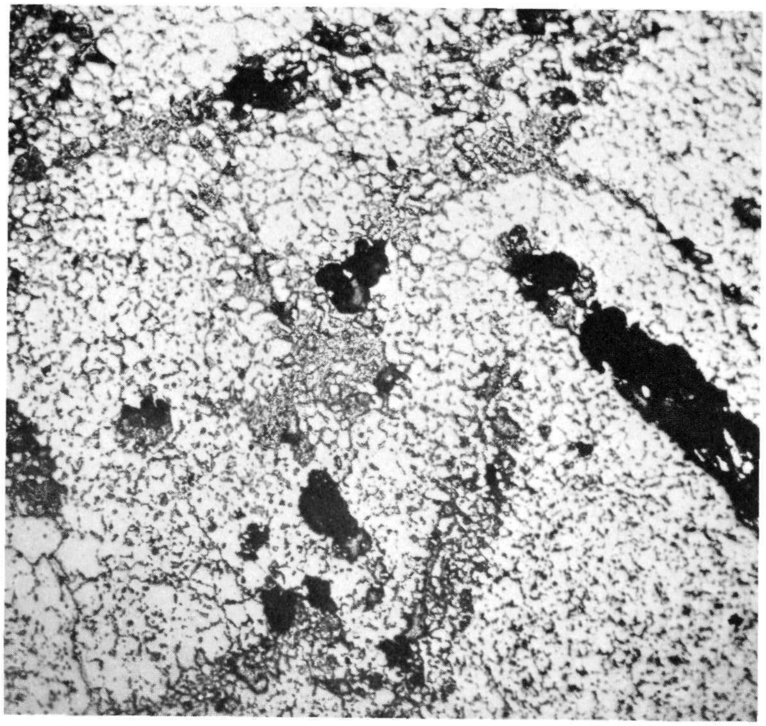

31290 50X

Figure 33. Reacted Niobium Fibers in Recrystallized Center of Specimen ANL-35-29.

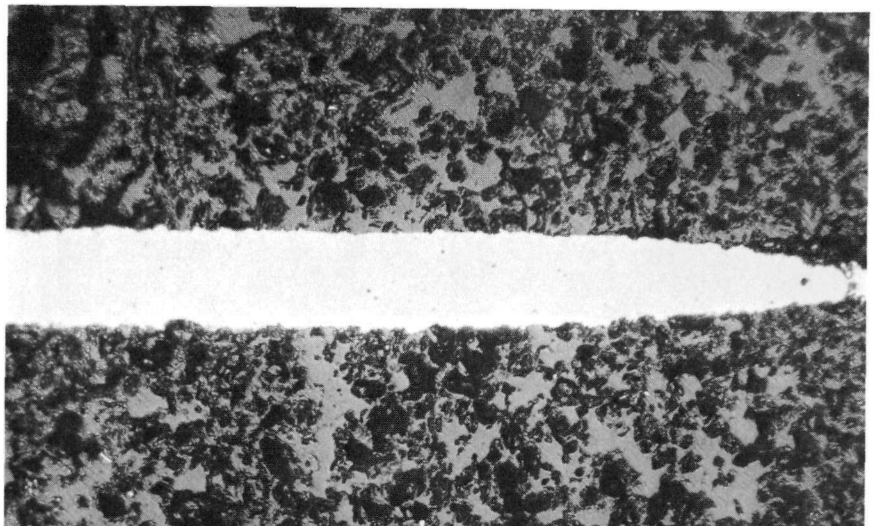

31310 250X

Figure 34. Unreacted Molybdenum Fiber in Specimen ANL-35-26.

The appearance of the clad specimens clearly showed that higher temperatures were achieved than in the bare pellets. This is predominantly attributed to the reduction of heat losses from the ends when the ratio of length to diameter was increased from one to two. The temperature drops through the cladding and bonding were also factors in increasing the temperature.

Unfibered, lead-bonded pellets (see Figures 35, 36, and 37) exhibited the normal central void and very large radial grains at high integral kdθ values, but only cracking at lower values. Lead was present in the center of ANL-35-28 and in the cracks of ANL-35-24, but not in the center of ANL-35-20, probably because no large radial fissures existed for its passage. Lead in the circumferential cracks of ANL-35-20 and ANL-35-28 caused an outer layer of oxide to slough off after repeated thermal cyclings, giving the pellet a triangular shape as it was restrained by the spacing ribs. Specimens ANL-35-20 and ANL-35-28 exhibited a pore structure similar to the platelet pores in ANL-35-5. Some of these pores, shown in Figure 38, are filled with lead which probably condensed from the vapor phase. In some specimens, the Zircaloy-2 spacing ribs were rounded and showed evidence of incipient melting on the surface adjacent to the pellet. This condition is indicative of a high irradiation temperature. Examples of this are specimens ANL-35-20 and ANL-35-28 with almost identical integral kdθ values of 67 and 68 w/cm, respectively. The absence of heat-transferring lead in the center of ANL-35-20 led to a higher temperature than in ANL-35-28, which did contain lead all the way to the center. The ribs in ANL-35-20 were accordingly rounded, whereas those in ANL-35-28 were not.

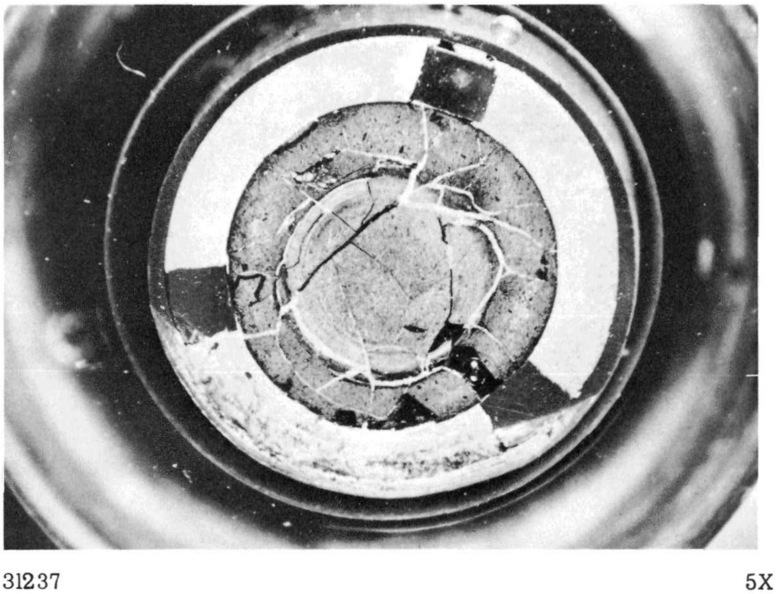

31237 5X

Figure 35. Polished Section of Unfibered Specimen ANL-35-24 after 4900 MWD/T at an Integral kdθ Value of 54 w/cm. Lead Has Entered the Cracks.

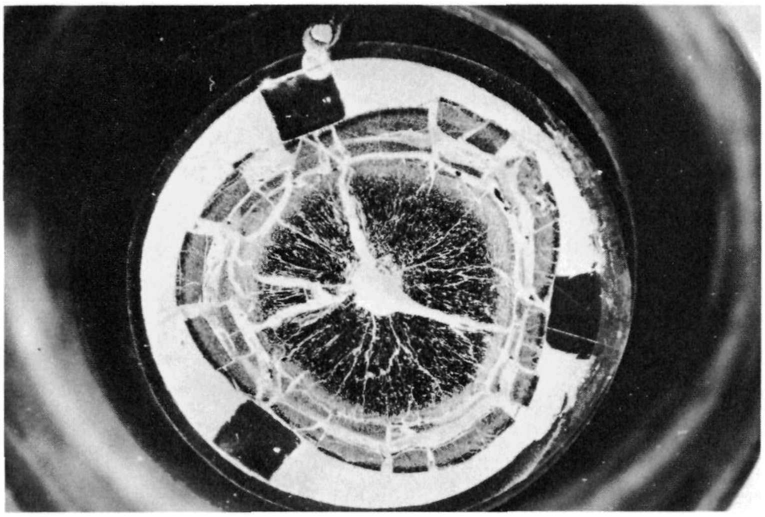

31242 5X

Figure 36. Polished Section of Unfibered Specimen ANL-35-28 after 11,300 MWD/T at an Integral kdθ Value of 68 w/cm. Lead in the Circumferential Crack Caused the Triangular Shape.

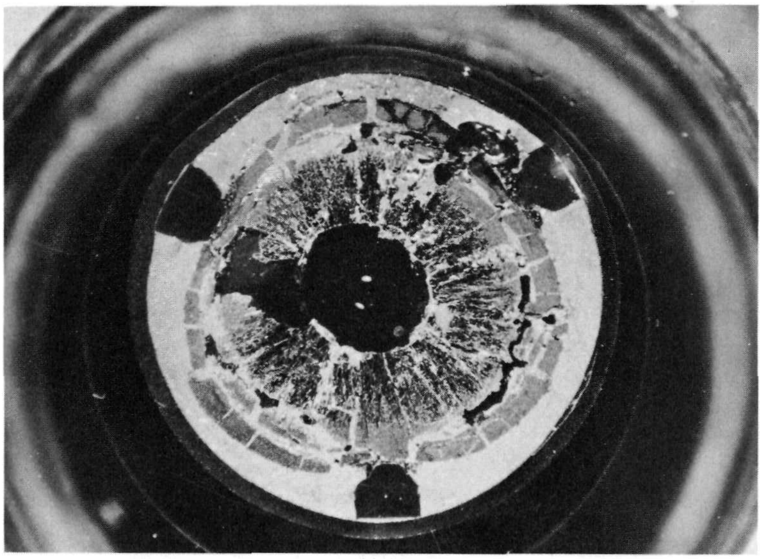

31230 5X

Figure 37. Polished Section of Unfibered Specimen ANL-35-20 after 20,000 MWD/T at an Integral kdθ Value of 67 w/cm. Lead Has Not Entered the Central Void.

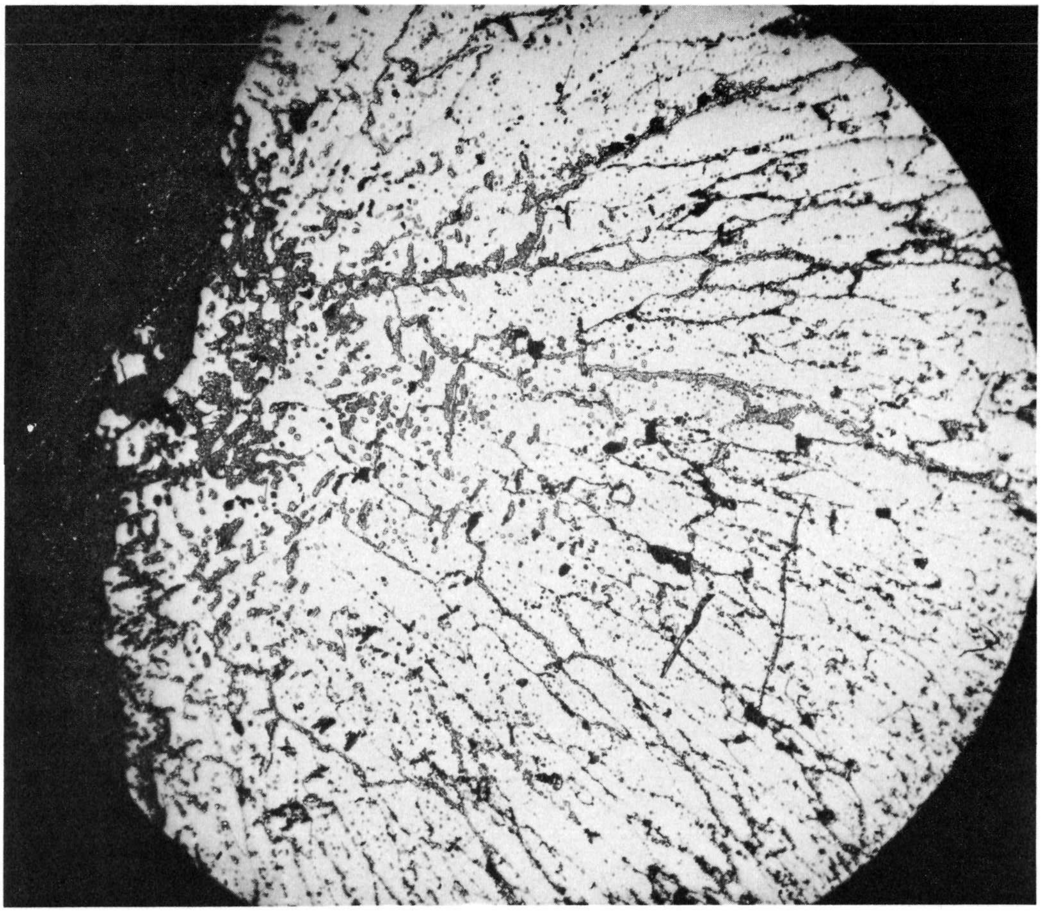

31314 50X

Figure 38. Columnar Grain Formation in ANL-35-28. Lead-filled Center Is at the Left. Note the Platelet Voids Near the Center.

It should be pointed out that the integral kdθ values are not absolute temperature indicators since the pellet surface temperatures, the lower limit of integration, were not known.

The lead-bonded fibered pellets exhibited neither symmetrical central voids nor large radially oriented grains. Central temperatures exceeded the melting point of molybdenum, 2620°C, and melted fibers were present in all specimens. Maximum observed central void formation occurred in ANL-35-18, shown in Figure 39, with an integral kdθ value of 122 w/cm. The void was irregularly shaped and contained lead and probably dissolved molybdenum, except in the very center which was open. This small central void was probably formed from the high internal gas pressure at the operating temperature. No extensive recrystallization was apparent in this specimen. Fibers were still discernible about one-third the distance to the center. The pellet surface temperature was sufficient to melt the Zircaloy-2 ribs to less than half their original thickness.

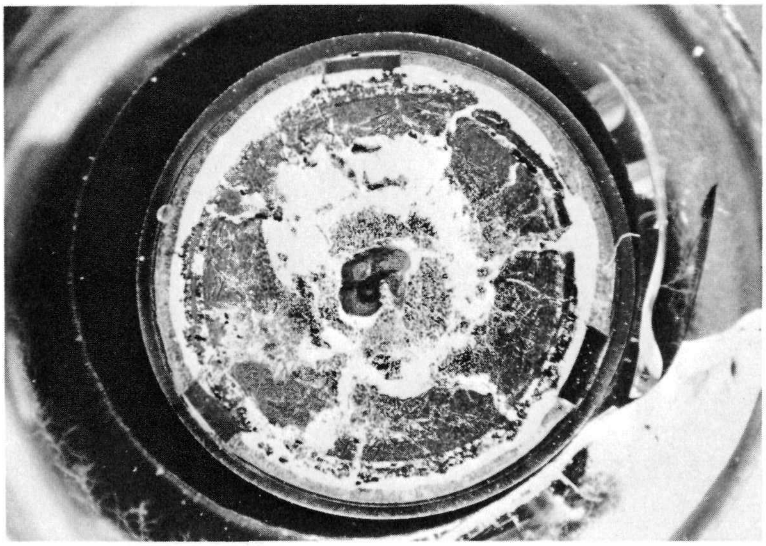

31229 5X

Figure 39. Polished Section of Molybdenum-fibered Specimen ANL-35-18 after 29,700 MWD/T at an Integral kdθ Value of 122 w/cm. White Areas Are Lead. Note the Reduction in Size of the Three Zircaloy-2 Ribs.

It should be noted that ANL-35-17 with a slightly higher integral kdθ value of 129 w/cm suffered catastrophic failure. An integral kdθ value of 100 w/cm in ANL-35-23 produced the structure shown in Figure 40. Here again lead had permeated to the center but left a small void.

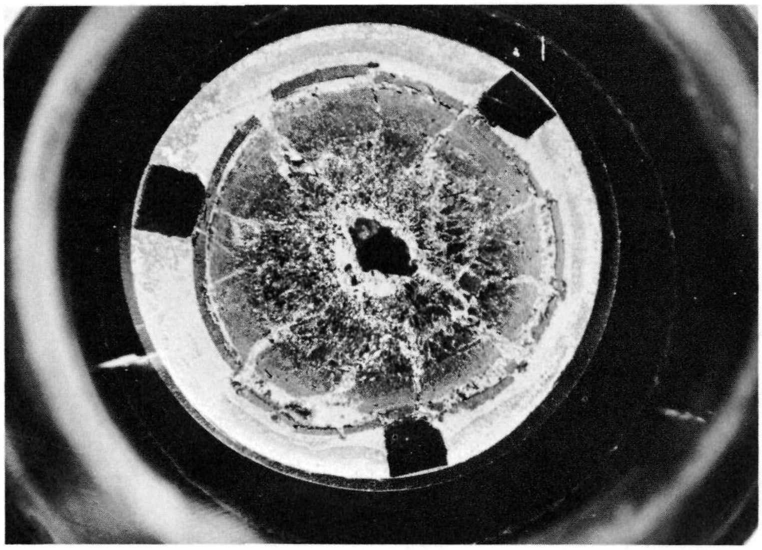

31236 5X

Figure 40. Polished Section of Molybdenum-fibered Specimen ANL-35-23 after 20,500 MWD/T at an Integral kdθ Value of 100 w/cm. Columnar Recrystallization Is Slight.

The oxide adjacent to the void (see Figure 41) was porous with spherical and platelet pores. There were small radially oriented grains behind the pores, but these ended where the fibers had not melted. Specimen ANL-35-26, having almost the same integral kdθ value as ANL-35-23 but containing 50 w/o UO_2, had the structure shown in Figures 42 and 43. These areas are just below a small central void that was present in the mating surface. The structure shown in Figure 43 is probably that of grains oriented parallel to the central axis of the pellet and in a lead matrix. The structure is similar to that of a perpendicular section through the oxide adjacent to the center void in ANL-35-23 (see Figure 41). No central void was formed in ANL-35-22 (see Figure 44), at an integral kdθ value of 83 w/cm. The central area contained equiaxed recrystallized grains and few melted molybdenum fibers. Figure 45 shows this central area with molybdenum in the grain boundaries. Unlike the formation of radially oriented grains in ANL-35-23, the formation of these equiaxed grains was not hindered by the presence of whole fibers. Melted fibers did not seem to impede either type of recrystallization.

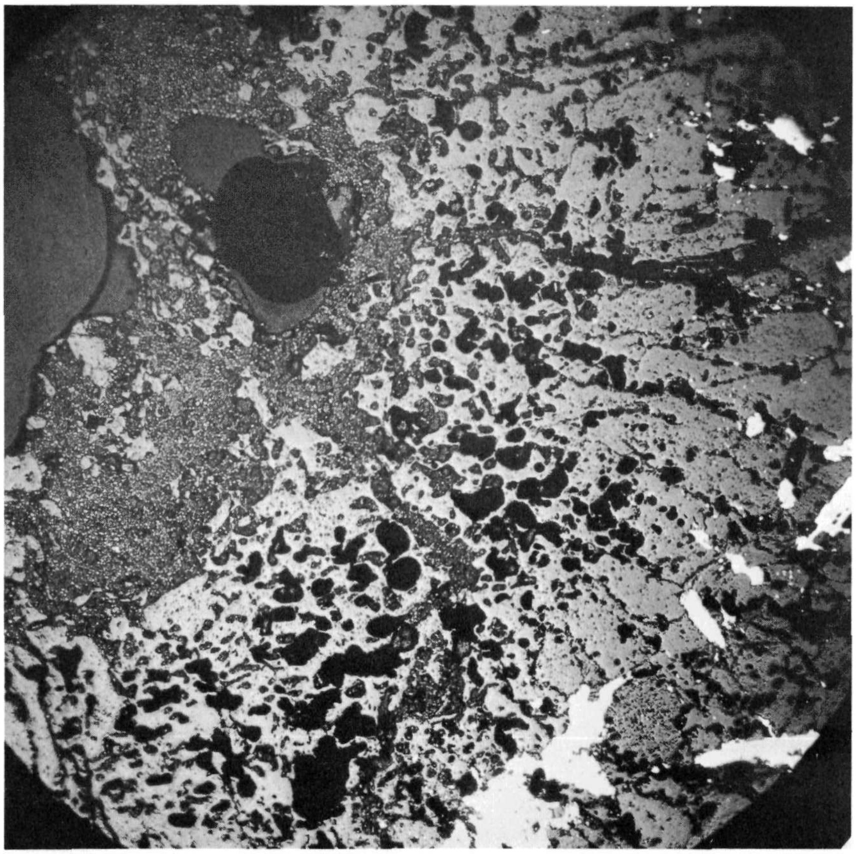

31285 50X

Figure 41. Area Adjacent to Central Void in Specimen ANL-35-23. Central Void is at Upper Left Surrounded by Lead. White Areas Are Melted Fibers.

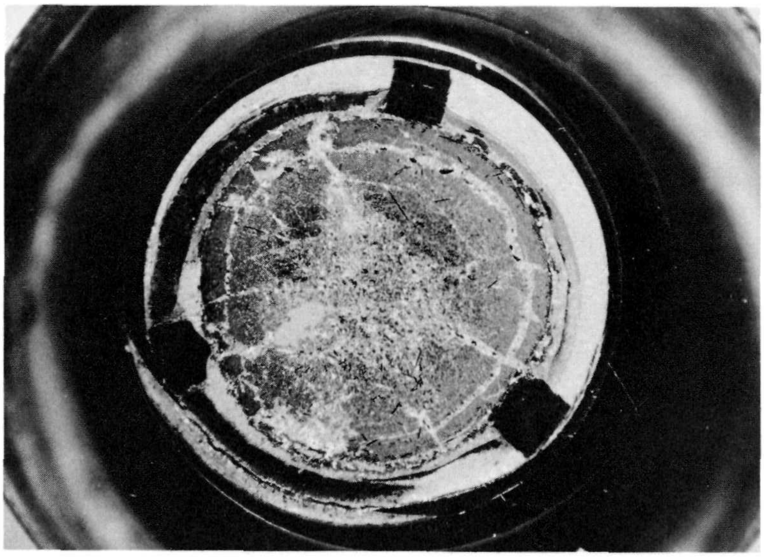

31241 5X

Figure 42. Polished Section of Molybdenum-fibered Specimen ANL-35-26 after 17,000 MWD/T at an Integral kdθ Value of 96 w/cm. Area Is Just below Central Void. Lead Has Permeated to Center.

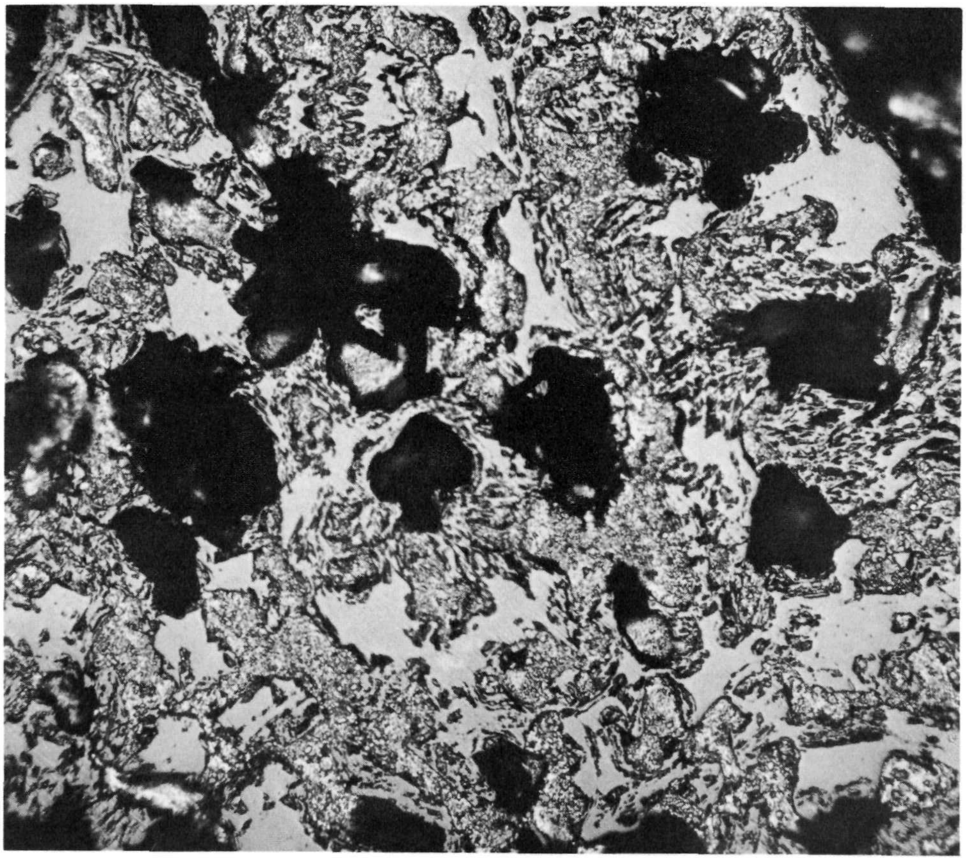

31309 250X

Figure 43. Center of Specimen ANL-35-26. Light Areas Are Oxide, Gray Fine Structure Is Lead, and Black Areas Are Voids.

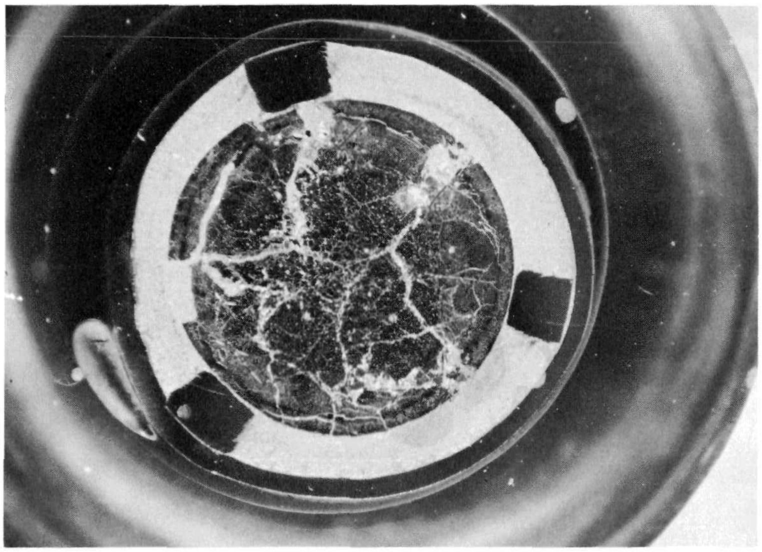

31235 5X

Figure 44. Polished Section of Molybdenum-fibered Specimen ANL-35-22 after 7100 MWD/T at an Integral kdθ Value of 83 w/cm. Central Area Is Equiaxially Recrystallized.

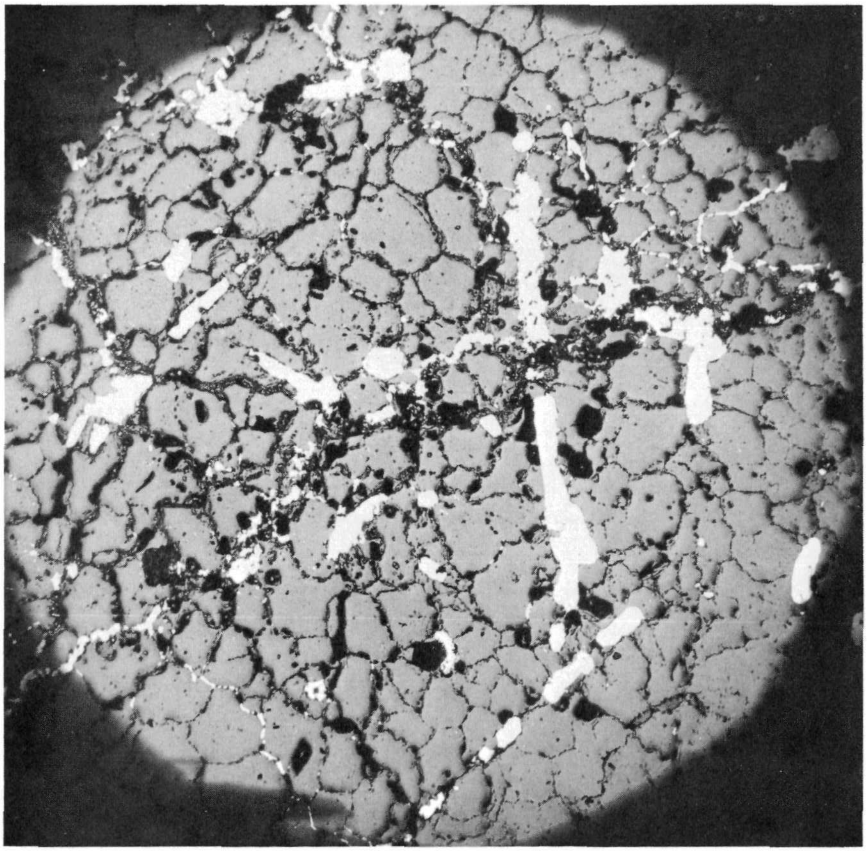

31278 50X

Figure 45. Center of Specimen ANL-35-22 Showing Equiaxed Grains and Partially Melted Molybdenum Fibers. Note the Breakup of the Fibers and Their Presence in Grain Boundaries.

Three helium-bonded, molybdenum-fibered specimens are shown in Figures 46 through 50. Two of the three specimens had central metallic spheres of molybdenum, and the fracture section of Figure 23 indicates that the third also had a small bead at the time of sectioning.

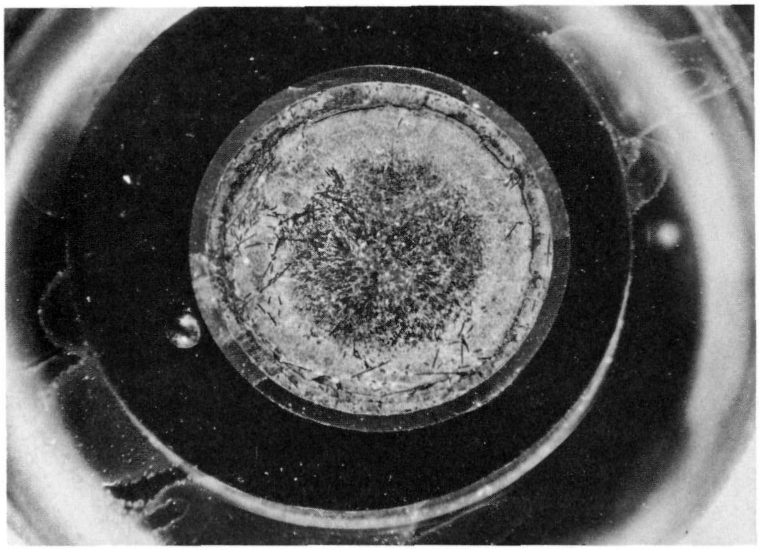

31239 5X

Figure 46

Polished Section of Molybdenum-fibered Specimen ANL-35-34 after 6800 MWD/T at an Integral $kd\theta$ Value of 78 w/cm. Area Is Just below the Metal Bead Shown in the Fracture Section of Figure 23.

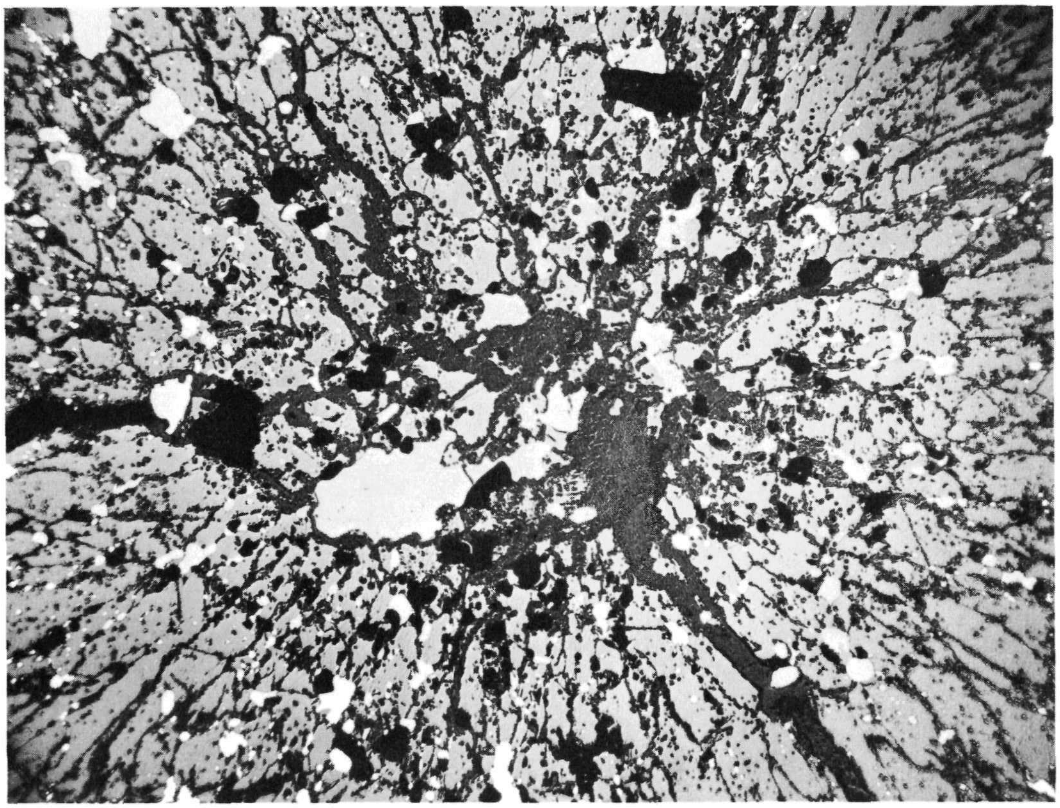

31296 50X

Figure 47. Center of Molybdenum-fibered Specimen ANL-35-34, Showing Remains of Small Metal Bead in the Center. Dark Gray Phase Is Mounting Material. White Phase Is Metal.

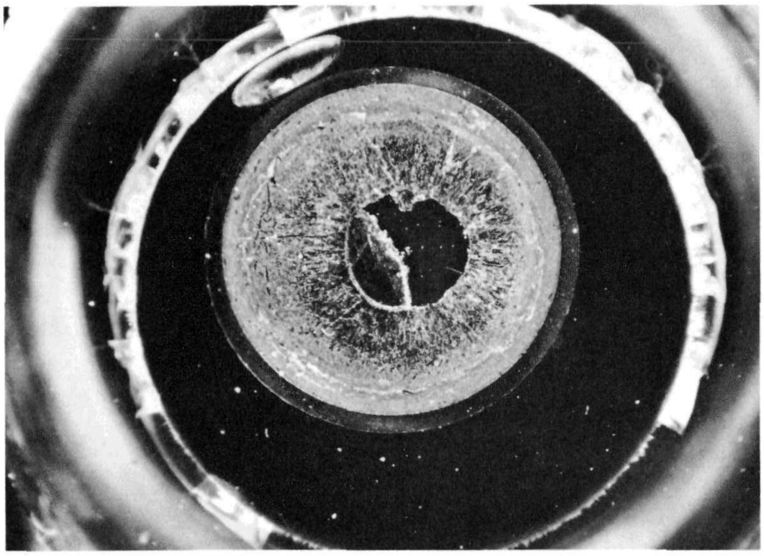

31231 5X

Figure 48. Polished Section of Molybdenum-fibered Specimen ANL-35-32 after 27,100 MWD/T at an Integral $kd\theta$ Value of 100 w/cm. Two-thirds of the Center Is Solid Metal Surrounded by Small Columnar Grains.

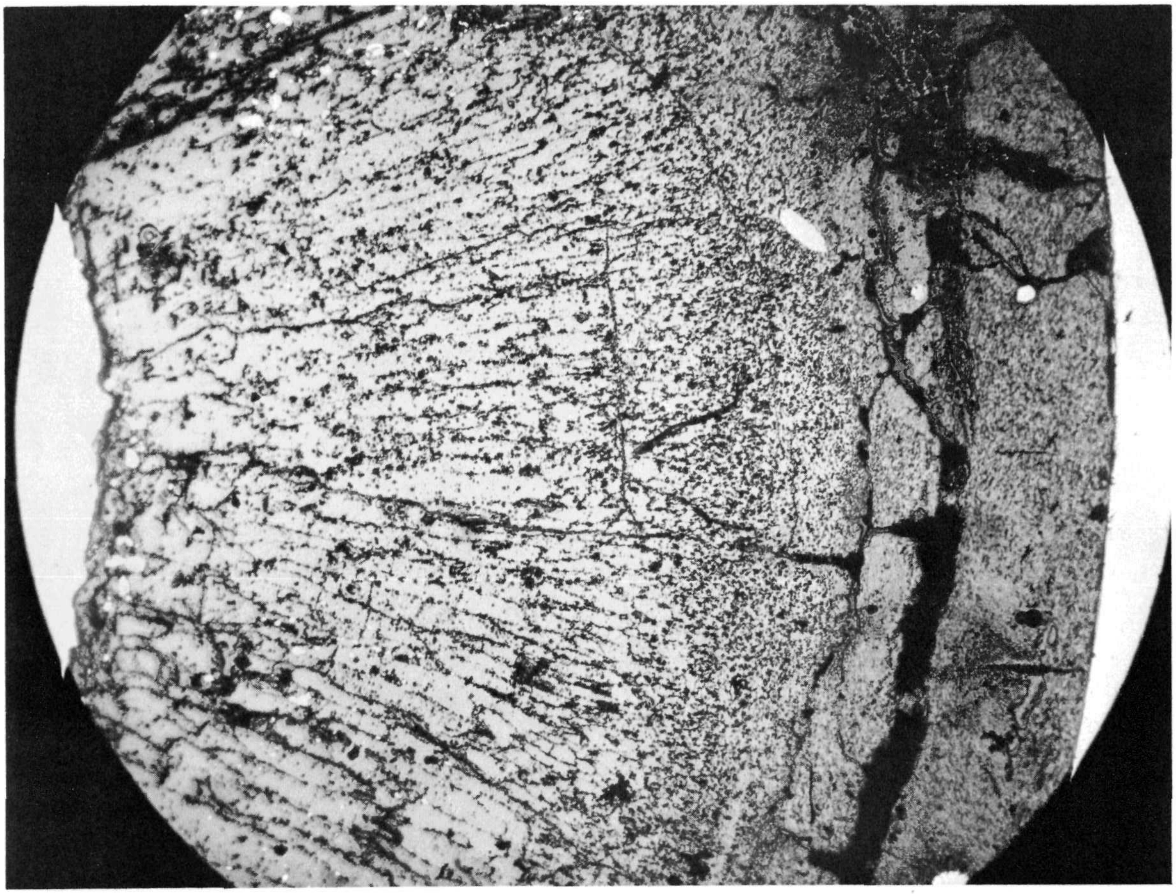

31252 50X

Figure 49. Columnar Grains in Specimen ANL-35-32. Metal Center Is at Extreme Left, Cladding at Extreme Right.

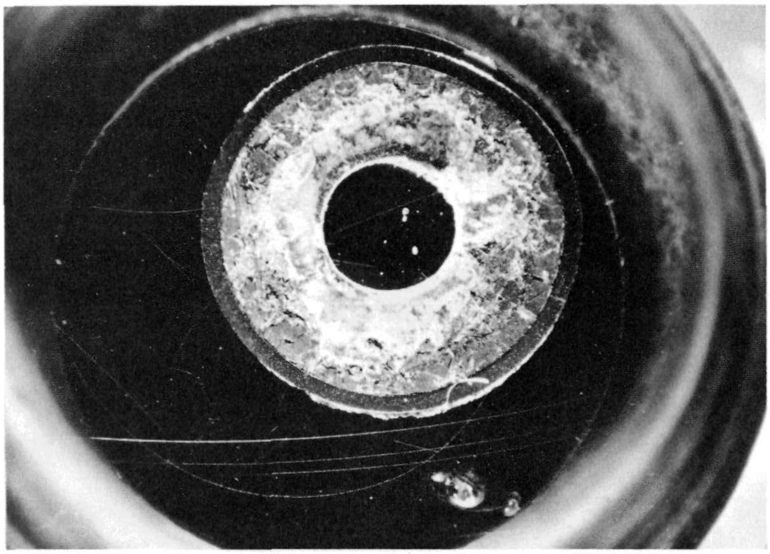

31232 5X

Figure 50. Polished Section of Molybdenum-fibered Specimen ANL-35-31 after 27,800 MWD/T at an Integral kdθ Value of 107 w/cm, Showing Solid Metal Center.

The recrystallization in ANL-35-34 had begun in an area of melted fibers, shown in Figure 47, and the metal had started to form a central bead. The area around the sphere in ANL-35-32 was depleted in fibers and the radial recrystallization was fairly extensive, as shown in Figures 48 and 49. The ceramic surrounding the sphere in ANL-35-31 was completely missing except at the extreme edges. This area had probably contained no fibers and had recrystallized, but was lost sometime between sectioning and mounting. The recrystallized grain size in ANL-35-32 was smaller than in the unfibered pellets (see Figure 38), but the pore structure, containing platelet voids, was similar. The second-phase material mentioned previously tended to segregate along grain boundaries after recrystallization.

DISCUSSION OF RESULTS

The results fall under the general headings of temperature effects and irradiation effects, and they will be discussed in that manner, although these topics are overlapping in many respects.

Temperature Effects

The improvement of thermal conductivity afforded by the fibers is in one way evidenced by the improved resistance to thermal shock. Unfibered pellets were severely cracked and fell apart during the irradiation period. Clad and unclad fibered pellets had much less tendency to crack. There is no doubt that the fibrous network played a major role in keeping the pellets together.

Both equiaxed and columnar recrystallization were observed in the fibered specimens. The equiaxed grains seemed unaffected by the presence of whole fibers. Columnar grains, however, were present only in areas where the fibers had melted and were the largest in specimens where the metal had migrated to the center. Even then, these large columnar grains were smaller than those in similarly recrystallized pellets containing no fibers. This would suggest that the mechanism for columnar recrystallization is hindered by the presence of a solid fiber.

Essentially, three mechanisms have been postulated for the formation of columnar grains and a central void in UO_2 fuels. Bates and Roake(16) suggest that the columnar grains are dendrites that have condensed from UO_2 vapor below the melting point of UO_2. This mechanism is supported by ex-reactor experiments in which these dendrites are shown to enclose platelet voids similar to those seen in our work. Bain and Robertson,(17) and Eichenberg et al.,(18) suggest that the columnar grains have solidified from a melt and that the central void is a solidification crater. Neither of these mechanisms can account for the results observed in our work in which metal fibers were present, even though center temperatures did exceed the melting point of the oxide in some cases.

The phenomena occurring in a fibered oxide are best explained by the mechanism proposed by Lawson and MacEwan(19) in which vaporization-condensation takes place across any small internal void where a large temperature gradient exists. The void then moves up the gradient to the center by vaporization-condensation on its opposite faces, growing in size as it encounters other voids. Its shape is that of a platelet and it sweeps out a columnar grain as it moves. The width of the grain is the width of the platelet and its boundaries contain tiny pores left at the ends of the advancing platelet where there is essentially no temperature gradient.

The evidence for this last mechanism has been pointed out in various parts of this report. The platelet voids were present at the termination of columnar grains, and the grain boundaries contained small spherical voids. It follows that a platelet void moving into a previously recrystallized grain that is free of voids should dissipate itself to the grain boundaries. The grain that was formed by this void would end in a point as do the outer columnar grains shown in Figure 38. Furthermore, a void movement as described requires a high localized temperature gradient. A solid fiber, being an excellent heat conductor, lessens the gradient, thus hindering void movement and thereby retarding recrystallization. A melted fiber, however, tends to break up, coalesce, and lose this heat-conducting capacity. The fact that columnar recrystallization did not begin until the fibers had melted, combined with the other evidence cited, supports the mechanism proposed by Lawson and MacEwan.

The formation of the central void by all the suggested mechanisms occurs because of the relocation of mass concurrent with the densification of the oxide. The net flow of solid mass is outward while the net flow of void space is toward the center. When metal fibers are present, the size of the central void is diminished or entirely absent in pellets with comparable heat ratings to unfibered pellets having central voids. Where appreciable central voids were formed at 67 w/cm in unfibered lead-bonded pellets, a much smaller void was first observed in a molybdenum-fibered pellet at 96 w/cm. Since columnar recrystallization was similarly retarded by fibers, the fibers must be retarding a single mechanism that creates both the columnar grains and the central void. This mechanism can only be the movement of voids by the sublimation process. It is evident, therefore, from the observed effects on recrystallization and central void formation, that the fibers have effectively increased the thermal conductivity of the oxide.

The presence of the molybdenum beads in the center of helium-bonded specimens can be explained by the void movement to the center. When the molybdenum melted, small voids could sweep to the center and form the large central voids, leaving columnar grains in their wake. Particles of liquid metal would be carried along with these voids because their high surface energies would "float" them in the moving voids. The metal particles would be deposited in the center of the pellet at the same time the central void was being formed. Surface tension would coalesce the metal to the observed spherical shape. The time and temperature dependence of the process is suggested by specimen ANL-35-34, irradiated for only 44 days at an integral $kd\theta$ value of 78 w/cm, in which only a small bead was formed with limited recrystallization around it. Without a very high temperature gradient to initiate and propagate the transport process, the voids and metal would be in temperature equilibrium and no movement would occur. The absence of the beads in the centers of lead-bonded specimens suggests that the lead, either by its presence in cracks or by its superior heat transfer to the cladding, reduced the high temperature gradients. Any molybdenum that did reach the center from close by areas was probably dissolved in boiling lead. It has been demonstrated that alloys with up to 20 w/o molybdenum can be prepared by dissolving molybdenum in boiling lead.(20)

Columnar recrystallization occurring above and below the central void and oriented axially will cause the ends of the pellet to become convex. Lengthening the fuel in this manner can be detrimental to the cladding. Since metal fibers retard columnar recrystallization, their use in oxide pellets could prevent this ratcheting effect.

The niobium reactions with the pellet environment lessens considerably its effectiveness in improving the thermal conductivity and retarding recrystallization and central void formation. At the time this investigation was initiated, in 1956, no information was available on the high-temperature compatibility of niobium with ThO_2 or UO_2. More recently, Kerr(21) has found that niobium undergoes a reaction with UO_2 at 2065°C but no reaction with ThO_2 up to 2135°C. He also found that molybdenum does not react with UO_2 up to 2155°C but does react with ThO_2 at this temperature. Gangler et al.,(22) however, found no reaction between niobium and UO_2 up to 2468°C, the melting point of niobium. Borchardt(23) found that niobium will reduce U_3O_8 at about 500°C and concludes that it is a solid-state reaction. We must conclude from our results that niobium does react with the ThO_2-UO_2 environment, either by a solid or gaseous mechanism or both. As previously mentioned, both oxygen and hydrogen were probably available to react with the niobium.

The molybdenum fibers exhibited no similar reactions. A molybdenum oxide reaction would have precluded the molybdenum deposition that was observed in the center of the helium-bonded specimens.

The effect of the bonding agent, lead or helium, in the annulus is clearly shown in the number of cladding failures and in the oxide microstructures. The microstructures indicated higher internal temperatures and steeper temperature gradients in the helium-bonded specimens. With the large metal bead in the center, the region of highest heat generation was effectively moved outward toward the cladding. Combining this with any small area of poor contact between cladding and oxide could cause the cladding to melt and fail. Lead bonding, however, did not generally change the region of highest heat generation and it tended to even out the heat flux. The failure of the one lead-bonded specimen was probably caused by boiling of the NaK coolant at the cladding surface and melting the Zircaloy-2 cladding, a result of a high rate of heat generation. This failure occurred at a heat rating of 129 w/cm, whereas the specimen that did not fail at 122 w/cm showed considerable melting of the supporting ribs. The first cladding burnout of a helium-bonded specimen occurred at a heat rating of 97 w/cm, and another showed indications of melting at 78 w/cm.

Irradiation Effects

The dimensional stability exhibited by the sound clad specimens agrees with previous findings for ThO_2-UO_2 solid solutions.(4) It is believed that the increase in cladding diameter of the failed specimens was partly caused by the high internal gas pressure and partly by the violent vaporization of NaK which seeped in through the cladding failure during reactor shutdowns and came in contact with the fuel.

The fission gas results were inconclusive for the intended purpose of comparing the release from fibered and unfibered pellets. The low irradiation temperature of the unfibered broken pieces makes a direct comparison impractical. It was thought that microcracks in the oxide, caused by the different thermal expansion of oxide and fiber, might yield ready paths for the escape of fission gas. These microcracks, however, were not prominent in the irradiated structure. The fission gas release from the fibered pellets is not high, if the burnup and irradiation temperatures are taken into consideration.

If there is indeed a change in the ratio of xenon to krypton release with increasing UO_2 content as the data suggest, it gives reason to believe that the xenon and krypton have different diffusion rates in the ThO_2-UO_2 solid solutions. The activation energies for diffusion of xenon and krypton in UO_2 are usually taken as the same, about 65 kcal/mol,(24) primarily because the experimental data are inadequate to distinguish between the two. However, it is reasonable to suspect that they do not diffuse at the same rate and their diffusion rates in ThO_2-UO_2 solid solutions would be affected by the ThO_2. The activation energy for diffusion of xenon in ThO_2 has been reported as 30 kcal/mol,(25) but as yet it is undetermined for krypton in ThO_2. It is probable that the krypton activation energy is also affected but to a different degree, giving the variable xenon/krypton ratio observed in this work.

The second phase that was present in all specimens may possibly be fission product oxides, a higher uranium oxide such as U_3O_8 or U_4O_9, or a CaF_2 precipitation. The presence of this phase did not seem to be detrimental to the irradiation behavior.

CONCLUSIONS

1. Molybdenum fibers effectively increase the thermal conductivity of ThO_2-UO_2 pellets and permit higher heat ratings than unfibered pellets before comparable thermal effects occur. The fibers tend to reduce central void formation, retard recrystallization, and maintain the integrity of the pellets.
2. Niobium fibers reacted with the ThO_2-UO_2 environment and their use was vitiated.
3. No evidence was found that fibers enhance fission gas release.
4. Lead bonding allows significantly higher heat ratings than helium bonding before cladding failures occur.

ACKNOWLEDGMENTS

The authors wish to acknowledge the work of F. Pausche, C. H. Gebo, and W. A. Ahrens who performed the postirradiation examinations. Appreciation is also expressed to B. D. Holt and C. E. Plucinski for the fission gas mass spectrographic analysis, and to R. J. Popek, A. L. Harkness, and C. M. Stevens for the uranium mass spectrographic analyses. The authors are especially indebted to J. H. Handwerk for assistance in having the specimens fabricated, to R. Carlander for developing the metallographic techniques, and to D. C. Hill for his stimulating and very helpful discussions of the results.

REFERENCES

1. Fieldhouse, I. B., and J. C. Hedge, ARF Project GO25D1 (July 1957).

2. Arenberg, C. A., Y. Baskin, and J. H. Handwerk, Thoria Base Metallo-Ceramics, TID-7530, Part 1 (April 1957).

3. Baskin, Y., Y. Harada, and J. H. Handwerk, Some Physical Properties of Thoria Reinforced by Metal Fibers, J. Am. Cer. Soc., 43, 489-492, (Sept. 1960).

4. Kittel, J. H., and J. H. Handwerk, Preliminary Irradiations of the Ceramic Fuels UO_2, UO_2-Zr and ThO_2-UO_2, ANL-5675 (1958).

5. Robertson, R. F. S., and V. C. Hall, Jr., Fuel Defect Test - Borax-IV, ANL-5862 (1959).

6. Robertson, R. F. S., Tests of Defected Thoria-Urania Fuel Specimens in EBWR, ANL-6022 (1960).

7. Baskin, Y., C. A. Arenberg, and J. H. Handwerk, Thoria Reinforced by Metal Fibers, Bulletin Am. Cer. Soc., 38 (No. 7), 345-348 (July 1959).

8. Lewis, W. B., Flux Perturbation by Material Under Irradiation, Nucleonics, 13 (10), 82-85 (Oct 1955).

9. Glasstone, S., Principles of Nuclear Reactor Engineering, p. 110, D. Van Nostrand Co., New York (1955).

10. Kittel, J. H., and S. H. Paine, Effects of High Burnup at Elevated Temperatures on Uranium-0.52 and 1.62 w/o Zirconium Alloys, ANL-5406 (1959).

11. Millsap, D. A., and J. M. Waage, RMF Measurements of Sample Fuel Plates, Quarterly Report MTR-ETR Technical Branches, Oct. 1 - Dec. 31, 1959, IDO-16620, pp. 8-10 (1959).

12. Taraba, F. R., Thermal Neutron Irradiation of Natural Thorium, ANL-5335 (July 1954).

13. Pletke, L., and G. Murphy, Temperature Distribution in a Metal Cylinder Containing a Heat Source, ISC-428 (1953).

14. Robertson, J. A. L., $\int k d\theta$ in Fuel Irradiations, CRFD-835 (1959).

15. Katcoff, S., Fission-Product Yields from Neutron-Induced Fission, Nucleonics, 18 201-208 (Nov 1960).

16. Bates, J. L., and W. E. Roake, Irradiation of Fuel Elements Containing UO_2 Powder, HW-60578 (1959).

17 Bain, A. S., and J. A. L. Robertson, UO_2 Irradiations of Short Duration, CRFD-825 (April 1959).

18. Eichenberg, J. D., P. W. Frank, F. J. Kisiel, B. Lustman, and K. H. Vogel, Effects of Irradiation on Bulk UO_2, WAPD-183 (Oct 1957).

19. Lawson, V. B., and J. R. MacEwan, Thermal Simulation Experiments with a UO_2 Fuel Rod Assembly, CRFD-915, (1960).

20. Hansen, M., Constitution of Binary Alloys, McGraw-Hill Co., New York (1958), p. 970.

21. Kerr, J. M., Compatibility of Various Oxides with Selected Metals, Oak Ridge National Laboratory Metallurgy Division Annual Progress Report for Period Ending September 1, 1959, ORNL-2839, pp. 292-294.

22. Gangler, J. J., W. A. Sanders, and I. L. Drell, Uranium Dioxide Compatibility with Refractory Metals, Carbides, Borides, Nitrides and Oxides Between 3500 and 5000°F, NASA-TN-D-262 (1960).

23. Borchardt, H. J., Observations on Reactions of Uranium Compounds, J. Inorg. and Nucl. Chem., 12, 113-121 (1959).

24. Cottrell, W. B., J. L. Scott, H. N. Culver, and M. M. Yarosh, Fission-Product Release from UO_2, ORNL-2935 (1960).

25. Matzke, Hj., and R. Lindner, Zeit Naturforsch. 15a, 647-8 (1960).